Agricultural and Forest Meteorology 311 (2021) 108692

Contents lists available at ScienceDirect

Agricultural and Forest Meteorology

journal homepage: www.elsevier.com/locate/agrformet

Modelling actual evapotranspiration using a two source energy balance model with Sentinel imagery in herbaceous-free and herbaceous-cover Mediterranean olive orchards

Sergio-D. Aguirre-García [a,b,*], Sergio Aranda-Barranco [a,b], Hector Nieto [c], Penélope Serrano-Ortiz [a,b], Enrique-P. Sánchez-Cañete [b,d], Juan-L. Guerrero-Rascado [b,d]

[a] University of Granada, Ecology Department, 18072 Granada, Spain
[b] Andalusian Institute Earth System Research IISTA–CEAMA, 18006 Granada, Spain
[c] Complutum Tecnologías de la Información Geográfica S.L. (COMPLUTIG), Colegios 2, 28801 Alcalá de Henares, Spain
[d] University of Granada, Applied Physics Department, 18072 Granada, Spain

ARTICLE INFO

Keywords:
Remote sensing
Multispectral Instrument
Sea land surface temperature Radiometer
Eddy covariance

ABSTRACT

Precipitation deficit and more extreme drought and precipitation events are expected to increase in the Mediterranean region due to global warming. A great part of this region is covered by olive orchards, representing 97.5% of the world's olive agricultural area. Thus, the adaptation of olive cultivation demands climate-smart management, such as the optimization of water use efficiency, since evapotranspiration is one of the most important components of the water balance. The novelty of this work is the combination of the remote sensing data fusion and the Two Source Energy Balance (TSEB) model (through Sentinel-2 and Sentinel-3 imagery) to estimate the actual daily evapotranspiration (ET_d), at high spatial (20 m) and temporal (daily) resolution, in an olive orchard under two management regimes: herbaceous free (HF) and herbaceous-cover (HC); along a three years period, based on the hypothesis that TSEB is still able to track and estimate the evapotranspiration over more complex canopies. The study was carried out from 2016 to 2019 in an olive orchard in the South of Spain, where the flux estimates were validated and assessed by in situ eddy covariance (EC) measurements. The results show better agreement in HC for net radiation (R_n) and the soil heat flux (G), but similar for both surfaces regarding the sensible (H) and latent (λE) heat fluxes, as well as ET_d. On both surfaces greater differences obtained at higher H, and the magnitude of overestimation of λE and ET_d were influenced by the EC energy imbalance. By contrast, G was overestimated with HC probably influenced by herbs, and equally underestimated for HF surfaces. The obtained results are in agreement with similar studies in tree crop orchards, and show the consistency of the used methodology and its usefulness for some farming activities, even on the more heterogeneous surface.

1. Introduction

In recent years, there has been an increase in impacts on the Earth ecosystems caused by weather and climate events amplified by climate change. These events produce displacement, migrations and important consequences on human health, socio-economic development, and food security (Kappelle et al., 2020; UNESCO and UN-Water, 2020). With the policy of net zero CO_2 emissions expected for 2055 and reducing the net non-CO_2 radiative forcing after 2030, global warming will probably (with a high degree of confidence) increase the global temperature between 1.5 °C (best-case scenario with a faster reduction of CO_2 emissions) to 2.0 °C (no reduction of net non-CO_2 radiative forcing) in upcoming decades (2030-2052) and last for centuries or millennia (Masson-Delmotte et al., 2018). Consequently, water availability will become more unreliable. Due to more extreme precipitation and drought events, precipitation deficits are likely in the Mediterranean region (Lionello and Scarascia, 2018; UNDRR, 2019; UNESCO and UN-Water, 2020). Presently, agriculture represents around 70% of global freshwater use (Shukla et al., 2019). Therefore, water resources and productivity maximization can play a very important part in

* Corresponding author.
E-mail address: sergiodag@ugr.es (S.-D. Aguirre-García).

https://doi.org/10.1016/j.agrformet.2021.108692
Received 7 June 2021; Received in revised form 13 October 2021; Accepted 16 October 2021
Available online 5 November 2021

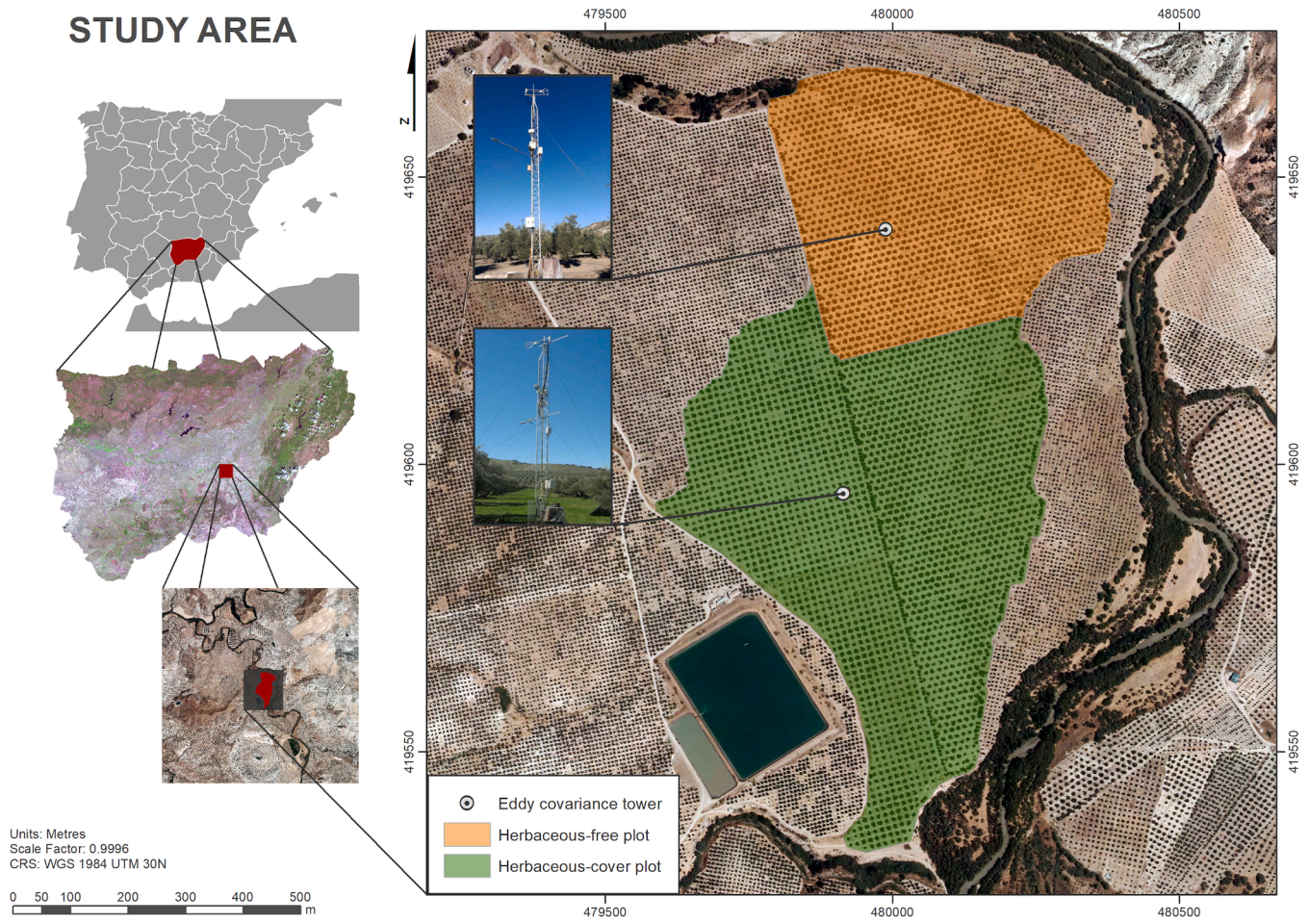

Fig. 1. Location and description of study area. Cartographic sources: Base cartography of the CNIG (National Spanish Centre for Geographical Information) BCN500; Orthoimage of the PNOA (National Plan of Aerial Orthophotography), study site at 0.5 m of spatial resolution of maximum timeliness, acquired from CNIG; Province of Jaén, Sentinel-2 (https://sentinel.esa.int/web/sentinel/sentinel-data-access, accessed 14 May 2021).

mitigating the effects of climate change. Sustainable management, including the maintenance of spontaneous herbaceous cover, can preserve land productivity and prevent and reduce its degradation. Moreover, it can reduce greenhouse gas emissions and help to sequester carbon in biomass and soils (Shukla et al., 2019; UNDRR, 2019; UNESCO and UN-Water, 2020).

One of the most important crops in the Mediterranean basin with relevant socio-economic benefits and ecological consequences are olive trees. The Mediterranean accounts for 97.5% (10.5 Mha) of the world's olive cultivation area (http://www.fao.org/faostat/en/#data/QC, accessed 14 May 2021). It occupies 2.7 Mha in Spain, of which more than 1.6 Mha are in Andalusia (MAPA, 2019). In this context, olive cultivation demands climate-smart management to facilitate crop adaptation to future climate scenarios and predictable development. Thus, management optimization and more efficient water use in relation to productivity is an especially important issue. Therefore, a better quantification of the components of the water balance in olive trees is essential. Evapotranspiration (*ET*) is one of the most important components of the water balance in which relevant decreases are expected in the Iberian Peninsula as consequence of climate change (García-Valdecasas Ojeda et al., 2020). Therefore, to improve the water use efficiency of agricultural systems there is a need to provide timely estimates of grove-scale *ET* and water use.

The latent heat flux (λE) or *ET* represents a latent energy transferred to the lower atmosphere later released in the form of clouds and precipitation. Different models have been developed during recent decades to estimate it (Courault et al., 2005; Kalma et al., 2008; Overgaard et al., 2006). Most of these models are based on the surface energy balance and mainly supported by the thermal infrared (TIR) data through remote sensing. Therefore, *ET* can be calculated from the λE as a residual from the energy balance, using estimations of net radiation (R_n), sensible heat flux (H) and soil heat flux (G), assuming that heat accumulated in the canopy, energy for photosynthesis, and advection are negligible ($\lambda E = R_n - H - G$). These models are based on the vertical transport of mass and heat exchange rate between the land surface and the atmosphere. These exchanges are regulated by land surface and vegetation properties, and driven by the local meteorology. Among them, one-source and two-source models have been developed. One-source models consider the surface as the single layer in heat and momentum exchange with the atmosphere without differentiating between radiative and turbulent exchange processes for the soil evaporation and vegetation components. Alternatively, two-source models consider a soil/substrate layer and a vegetation canopy layer interacting with the atmosphere.

Flux partitioning between layers (soil and canopy) can be especially complex when they exhibit a high degree of heterogeneity or strongly clumped canopies, such as in semiarid environments or widely spaced row crops, where both soil and vegetations layers will attain significantly different temperatures. Thus, two-source models such as Shuttleworth and Wallace (1985) have been developed with the aim of overcoming the limitations of one-source models which do not account for unique differences in exchange processes between soil/substrate and plant canopy. Similarly, Norman et al. (1995) and Kustas and Norman (2000) presented a Two-Source Energy Balance model (TSEB) that combines remote sensing and meteorological data for estimating

soil/substrate and plant canopy. It is based on directional (i.e., view geometry) radiometric surface temperature and partitions energy fluxes into soil (evaporation) and vegetation (transpiration). As opposed to one-source models, TSEB physically relates the radiometric temperature (T_{rad}), acquired with thermal infrared sensors, with the aerodynamic temperature required to accurately derive *H*, without the need for including any empirically related excess resistance formulation used in one-source models (Kustas et al., 2016). However, one of the challenges in application of TSEB is that canopy structure and the separation of total Leaf Area Index (*LAI)* between its green and senescent components can significantly influence output and difficult to determine from routine earth observations (Guzinski et al., 2013). However, it has proven to be a robust and versatile model, providing similar or better results than one-source models (e.g., Guzinski et al. 2020).

In the last decade, there has been an increase in studies using these remote sensing approaches to estimate *ET* in different biomes (García et al., 2013; Pakparvar et al., 2014), agro-ecological zones (Carpintero et al., 2020; Jaafar and Ahmad, 2020; Nyolei et al., 2019; Pasqualotto et al., 2019), crops (Bisquert et al., 2016; French et al., 2020; Gavilán et al., 2019; Le Page et al., 2014; Mokhtari et al., 2019), and more specifically on olive orchards (Cammalleri et al., 2010; Cammalleri et al., 2013; Fuentes-Peñailillo et al., 2018; Hoedjes et al., 2008; Olivera-Guerra et al., 2017; Ortega-Farías et al., 2016; Paço et al., 2014; Pôças et al., 2014). However, there is still a lack of operational TIR sensors on satellite platforms with both adequate temporal (i.e., daily) and spatial (i.e., $<$ 100 m) resolutions. For that reason, there have been proposed thermal sharpening and flux disaggregation techniques (Chen et al., 2014; Gao et al., 2012; Norman et al., 2003; Zhan et al., 2013), which combine different imagery sources and generate acceptably useful information at the field and orchard -scale. One recent and relevant improvement is the data fusion of optical Sentinel-2 (S2) and thermal Sentinel-3 (S3) imagery (Bellvert et al., 2020; Guzinski et al., 2020; Guzinski and Nieto, 2019) which allows the estimation of *ET* at both high spatial and temporal resolutions.

Although TSEB accounts for a single vegetated layer, this study is based on the hypothesis that TSEB, in particular the Guzinski et al. (2020) Sentinel-based *ET*, is still able to track and estimate *ET* over more complex canopies such as orchards with herbaceous cover. Previous application of TSEB with an interrow cover crop in vineyards was shown to provide reliable results (Knipper et al., 2020). This study aims to (1) model evapotranspiration through satellite remote sensing data on an olive orchard under two management regimes: maintenance of herbaceous cover and herbaceous suppression (bare soil); (2) to validate model output using ground-based measurements and assess the reliability of the methodology in these types of canopies; and (3) assess the effect of the herbaceous-cover on olive grove *ET*. For this purpose, we have applied the method proposed by Guzinski et al. (2020) for three hydrological years, from October 2016 to September 2019 in an olive orchard under the two types of understories.

2. Materials and methods

2.1. Study area

The study area is surrounded by great extensions of olive groves. It is located at the Southern Iberian Peninsula in the province of Jaén in Andalusia, Spain (Fig. 1), at 370 m elevation above sea level. The area has a Mediterranean climate. From 2000 to 2020 the near meteorological station of Andalusian Agroclimatic Information Network in Úbeda, sited at 37.9427º N, 3.3002º W and 343 m elevation above sea level, registered daily mean values of temperature 16.1 ºC, relative humidity 61.9%, solar radiation 17.8 MJ/m^{2}d, wind speed 0.7 m/s (predominantly coming from between north-east and south-east at night and from south-west during daytime); an annual accumulated average precipitation of 470.6 mm (33%, 36%, 26% and 5% fallen during autumn, winter, spring and summer, respectively); and an annual accumulated average reference evapotranspiration of 1199.1 mm.

The site consists of an irrigated olive grove (*Olea europaea L.*) divided into two flat plots (36.5 ha and 21.17 ha) over a clay loam texture soil (clay 44%, silt 32% and sand 24%) with a content of organic matter of 2.9% in the first 5 cm depth and 2.4% from 5 to 15 cm. One of the plots has a spontaneous herbaceous cover (HC) and the other is herbaceous-free (HF, treated with herbicide). The olive trees (around 80 years old) are distributed in a plantation frame of 12×12 m, and their crown height is 4 m approximately. Trees are drip irrigated at a rate of 32 l/h for 5-8 hours at night 3 times a week from March to October.

2.2. Ground-based data and validation

The two plots have one Eddy Covariance (EC) (Dabberdt et al., 1993) tower each, 9 m tall and separated by 466 m. Each tower supports a three-axis sonic anemometer (CSAT-3, Campbell Scientific, Logan, UT, USA) and an enclosed path infrared gas analyser (IRGA, Li-Cor 7200; Lincoln, NE, USA), together with complementary sensors to measure R_n and *G*, among other variables (Chamizo et al., 2017). EC data (wind speed components, temperature and water vapour density measured at 10 Hz) were processed using the software EddyPro 6.2.1 (LI-COR Inc, Lincoln, Nebraska, USA) to obtain half hourly fluxes of λE and *H*. Double coordinate rotations, time-lag compensation, and spectral corrections for high frequency range according to Moncrieff et al. (2004) were applied. Data at 10 Hz were subjected to statistical tests to detect and eliminate peaks, dropouts and incoherent or low variance values with respect to instrument resolution (Vickers and Mahrt, 1997). The upwind footprint that contributes to the measured exchanges was calculated based on the anemometer height, atmospheric stability, and surface roughness (Kljun et al., 2004). Tests of stationarity and turbulence development were applied to *H* and λE following Mauder et al. (2013), providing the flag "0" for high-quality fluxes (differences $<$ 30% for both tests), "1" for intermediate quality fluxes (differences $<$ 30% for one test), and "2" for poor quality fluxes (differences $>$ 30% for both tests). Only fluxes with quality 0 and 1 were used for this study. R_n was measured by a 4-component radiometer at 5 m height and *G* by heat plates at 0.8 m depth (see Chamizo et al. (2017) for details and instrumentation). The obtained data were subsequently filtered to eliminate those collected when power outages or drops or instrumentation malfunctioning. After filtering, the available data for validation on HF were 31.9% for *H* and 18.1% for λE, whereas for R_n and *G* were 71% and 87.6%, respectively. For HC, the available data were 31.3% for *H*, 15.3% for λE, 69.4% for R_n and 62.0% for *G*.

In order to determine EC daily *ET* (ET_d) data gaps in EC data were filled using the marginal distribution sampling technique described by Reichstein et al. (2005). From the EC data in the compared days, the available λE values on HF were the 39.5% and the filled ones the 60.5%, whereas on HC the available ones were the 41.3% and the filled ones the 58.7%. Later, for each day all λE corresponding to each 30-min period were averaged and transformed to mm/day.

2.3. Sentinel data

Two types of Sentinel products were used in this study. On one hand, S2 Level 1C Top Of Atmosphere (TOA) Multispectral Instrument (MSI) reflectances (S2MSI1C) (https://earth.esa.int/web/sentinel/user-guides/sentinel-2-msi/product-types/level-1c, accessed 14 May 2021) onboard both A and B S2 satellites. The S2MSIL1C product is processed and offered by the European Space Agency (ESA) as geometric ortho-corrected 100 square km tiles, projected in UTM/WGS84 at 10, 20 or 60 m of nominal spatial resolution depending on the spectral band. The MSI sensor has 13 bands centred from 442.3-443.9 to 2185.7-2202.4 nm wavelengths, providing imagery at 5-day revisit frequency, considering the constellation of both satellites (A and B) (Drusch et al., 2012; Gatti et al., 2018; https://sentinel.esa.int/web/sentinel/user-guides/sentinel-2-msi, accessed 14 May 2021). This imagery was used to sharpen

Table 1
Look-up table used by the model to extract the structural parameters of vegetation according to type of cover. Code is the code for land cover type; Description is the nominal for land cover type; HC max is the maximum canopy height (m, considered constant of 4 for olive orchards); f_C is the fraction of covered surface by the green canopy and represent the clustering level of the canopy ($f_C = 1$ for a homogeneous canopy); WC is a factor shape of tree's crown based on width / height ratio; Leaf width (m) is the typical size of the leaf; X_{LAD} is the Campbell (1990) angular distribution function coefficient of the leaves ($X_{LAD} = 1$ for a spherical distribution, $X_{LAD} < 1$ for erectophilic foliage).

Code	Description	HC max	f_C	WC	Leaf width	X_{LAD}
HF	Herbaceous-free	4	0.3	0.5	0.02	1
HC	Herbaceous-cover	4	0.4/0.9	0.5	0.02	1

thermal data and characterize the vegetation state. On the other hand, S3 Level-2 Land Surface Temperature product (SL_2_LST) (https://sentinel.esa.int/web/sentinel/user-guides/sentinel-3-slstr/product-types/level-2-lst, accessed 14 May 2021) is acquired by the Sea and Land Surface Temperature Radiometer (SLSTR) sensors onboard S3 A and B satellites. Likewise, this product is processed and offered by ESA at 1 km nominal spatial resolution. The S3 mission has a revisit frequency lower than a day (0.9 at equator and 0.8 at latitude higher than 30°) considering both satellites (A and B) (Donlon et al., 2012; https://sentinel.esa.int/web/sentinel/user-guides/sentinel-3-slstr, accessed 14 May 2021).

2.4. Ancillary data

Ancillary data required for running in TSEB with Sentinel data includes topography, land cover/land use and meteorology. Firstly, a Digital Elevation Model (DEM) obtained from the Shuttle Radar Topography Mission (http://srtm.csi.cgiar.org/srtmdata/, accessed 14 May 2021) at 30 m of spatial resolution was used. Secondly, air temperature at 2 m height (T_A) is resampled and extrapolated at 100 m above the DEM surface by a standard lapse rate of 6.5 K/km (Guzinski et al., 2020), dew point temperature at 2 m height, wind speed at 10 m height, incoming surface radiation, atmospheric pressure and Total Columnar Water Vapour content (TCWV), all them obtained from the ERA5 Reanalysis dataset (https://confluence.ecmwf.int/display/CKB/ERA5%3A±data±documentation, accessed 14 May 2021) produced by the European Centre for Medium-range Weather Forecast (https://www.ecmwf.int/en/forecasts, accessed 14 May 2021); and Aerosol Optical Depth (AOD) obtained from the Copernicus Atmosphere Monitoring Service (Morcrette et al., 2009; https://atmosphere.copernicus.eu/, accessed 14 May 2021) were considered as meteorological forcing data. Crop characteristics were assigned based on the land cover, whose map (SIGPAC) was obtained from the Andalusian Geographical Information System of Agricultural Smallholdings (https://www.juntadeandalucia.es/organismos/agriculturaganaderiapescaydesarrollossostenible/areas/politica-agraria-comun/paginas/sigpac-descarga-informacion-geografica-shapes-provincias.html, accessed 14 May 2021). Surface structural characteristics in TSEB were parameterised into a Look-up table (Table 1). We used this Look-Up Table to model more accurately the different fraction of covered surface by the canopy (f_C) on HC depending on dates of processing throughout the year, from $f_C = 0.4$ when herbaceous crop cover presence is residual to $f_C = 0.9$ when this cover is at maximum vigour.

2.5. Modelling processes

In order to model the energy balance components, the Two-Source Energy Balance model is run with the Priestley-Taylor approximation for the initial canopy transpiration assuming an unstressed canopy (TSEB-PT) (Kustas and Norman, 1999; Norman et al., 1995). The model provides estimates of the surface energy balance components of the soil and vegetation at 20 m of spatial resolution and daily temporal resolution, depending on S2 and S3 images availability and cloud-free conditions.

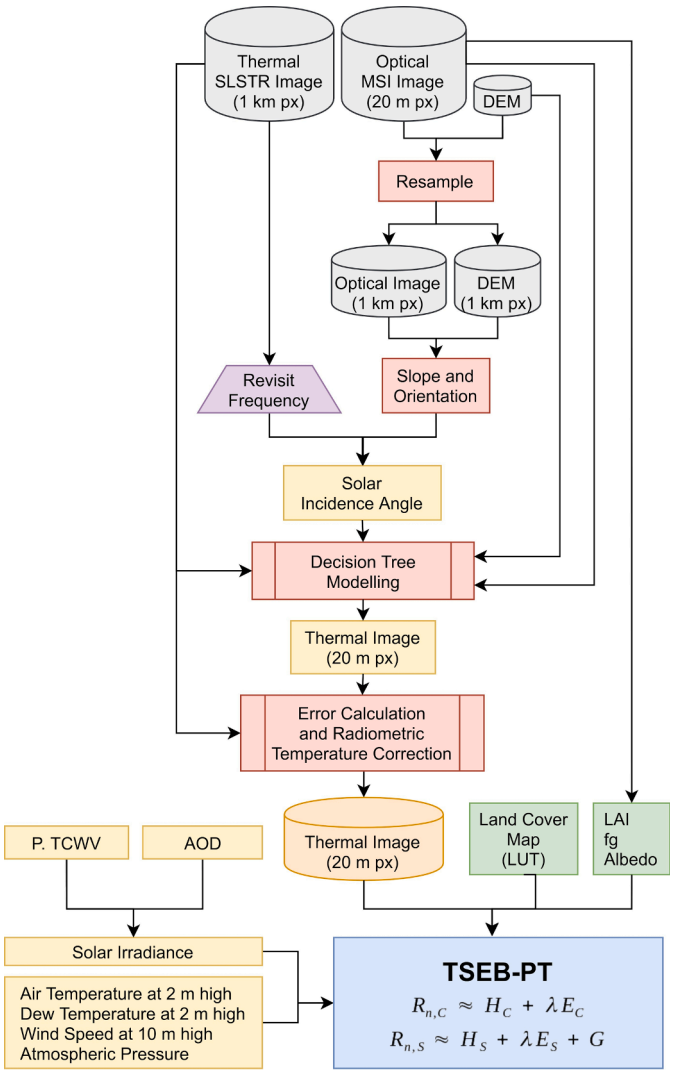

Fig. 2. Process Flow. DEM: Digital Elevation Model; P. TCWV: Pressure of Total Column Water Vapour; AOD: Aerosol Optical Depth; Land Cover Map (LUT): Look Up Table of Crop Characteristics; LAI: Leaf Area Index; fg: Green vegetation fraction, able to transpire; Albedo as leaf bi-hemispherical reflectance and transmittance for visible and near infrared; $R_{n,C}$ & $R_{n,S}$: Canopy & Soil Net Radiation fractions; H_C & H_S: Canopy & Soil Sensible Heat fractions; λE_C & λE_S: Canopy & Soil Latent Heat fractions; G: Soil Heat Flux.

First, the algorithm (Fig. 2) obtains high-resolution surface temperature images by the thermal image sharpening method (Gao et al., 2012; Guzinski and Nieto, 2019), which source code is available through GitHub (https://github.com/radosuav/pyDMS, accessed 14 May 2021). It takes advantage of the statistical relationships between optical and thermal datasets by combining each S3 scene with an S2 scene no more than four days apart. The S2MSI1C images are converted to bottom of the atmosphere (BOA) atmospherically corrected reflectances using the Sen2Cor (v2.5.5 for this study; https://step.esa.int/main/third-party-plugins-2/sen2cor/, accessed 14 May 2021) atmospheric correction processor (Louis et al., 2016). Afterwards, surface elevation, and solar incidence angle at the tilted surface, derived from the DEM at 30 m together with the S2 optical data at 20 m are resampled at the 1 km spatial resolution of the S3 SLSTR sensor to be used as predictors in a set of decision trees, in which the surface T_{rad} is considered the dependent variable. For model training, only 80% most

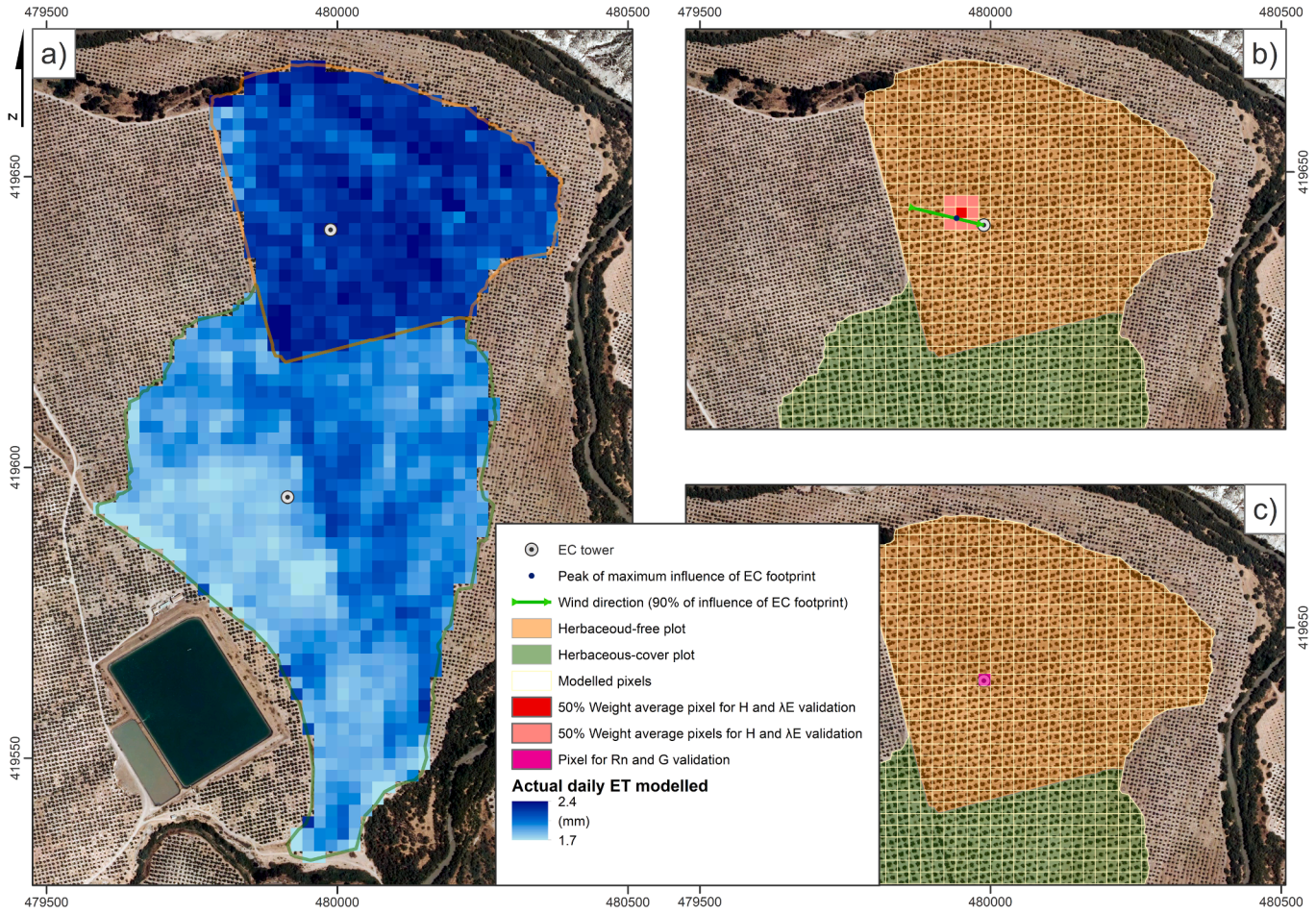

Fig. 3. Output of model for 2016-10-11 and example of validation vs. the EC data collected at the S3 overpass time. Modelled pixel values averaged for ET_d (a); pixel values used and weight-averaged according to the EC footprint calculated (see section 2.2) and footprint model described in Schmid (2002) (b); pixel value used to validate R_n and G (c).

homogeneous pixels at the 1 km scale are automatically selected as training samples. For each S2-S3 image pair, both local (using a moving window of 30 by 30 1 km pixels) and global (using the whole S2-S3 image extent) models are trained and subsequently combined into a regression model between T_{rad} and the predictors by weighting the local and global models based on the error predictions at coarse resolution (see Gao et al. (2012) and Guzinski et al. (2020) for further details of the Data Mining Sharpener). The trained model is then applied to the entire S2 scene at the original resolution of 20 m, producing a thermal sharpened image at this scale. Lastly, to guarantee the conservation of energy between the sharpened and original thermal images, a final correction is done by comparing the long-wave blackbody emission between the sharpened T_{rad}, aggregated at 1 km, and the original T_{rad} at 1 km. Thus, any residual bias is removed by recalculating the bias-corrected T_{rad} by adding an offset to all high-resolution sharpened pixels within each low-resolution pixel.

Secondly, the SEN-ET model implementation (Guzinski and Nieto, 2019) obtains all meteorological data at regional scale. Then, instantaneous clear-sky solar irradiance (SI_i) is calculated according to Perez et al. (2002) using *AOD, TCWV* and the solar zenith angle (*SZA*) at satellite overpass. Leaf area index (*LAI*), fraction of absorbed photosynthetically active radiation (*fAPAR*), canopy chlorophyll content (*CCC*) and canopy water content (*CWC*) (herb layer included) are obtained through the biophysical processor of S2 toolbox of SNAP software (v7.0.4 for this study; http://step.esa.int/main/toolboxes/snap/, accessed 14 May 2021) (Weiss and Baret, 2016). Leaf bi-hemispherical reflectance and transmittance for visible and near infrared are estimated from leaf chlorophyll concentration ($Cab = CCC / LAI$) and equivalent water thickness ($Cw = CWC / LAI$) respectively, based on regression curves calibrated using simulations of Prospect-D model (Féret et al., 2017). The estimated leaf spectra together with S2 *LAI* and tabulated values of soil spectra, and leaf angle distribution (X_{LAD}) from Table 1 are used to estimate net short wave radiation for soil and canopy layers according to the Campbell and Norman (1998) radiation transfer model and described in more detail in Parry et al. (2019).

The green vegetation fraction able to transpire (f_g) is calculated according to Fisher et al. (2008) as

$$f_g = \frac{fAPAR}{fIPAR} \tag{1}$$

where the fraction of intercepted photosynthetically active radiation (*fIPAR*) is estimated following Eq. 2

$$fIPAR = 1 - exp\left(-0.5\frac{LAI}{cos(SZA)}\right) \tag{2}$$

Afterward, the TSEB-PT model (Norman et al., 1995) is applied using the sharpened thermal data at 20 m, and meteorological, biophysical, land cover and crop structural variables for each image as main inputs. The TSEB-PT model version used in this study is available in source code at the GitHub repository (https://github.com/hectornieto/pyTSEB, accessed 14 May 2021). TSEB-PT focuses on the estimation of instantaneous R_n, H, and G and, partitioning the surface energy fluxes and T_{rad} between soil and vegetation sources, calculates instantaneous λE as the residual of the surface energy balance ($\lambda E = R_n - H - G$). Therefore,

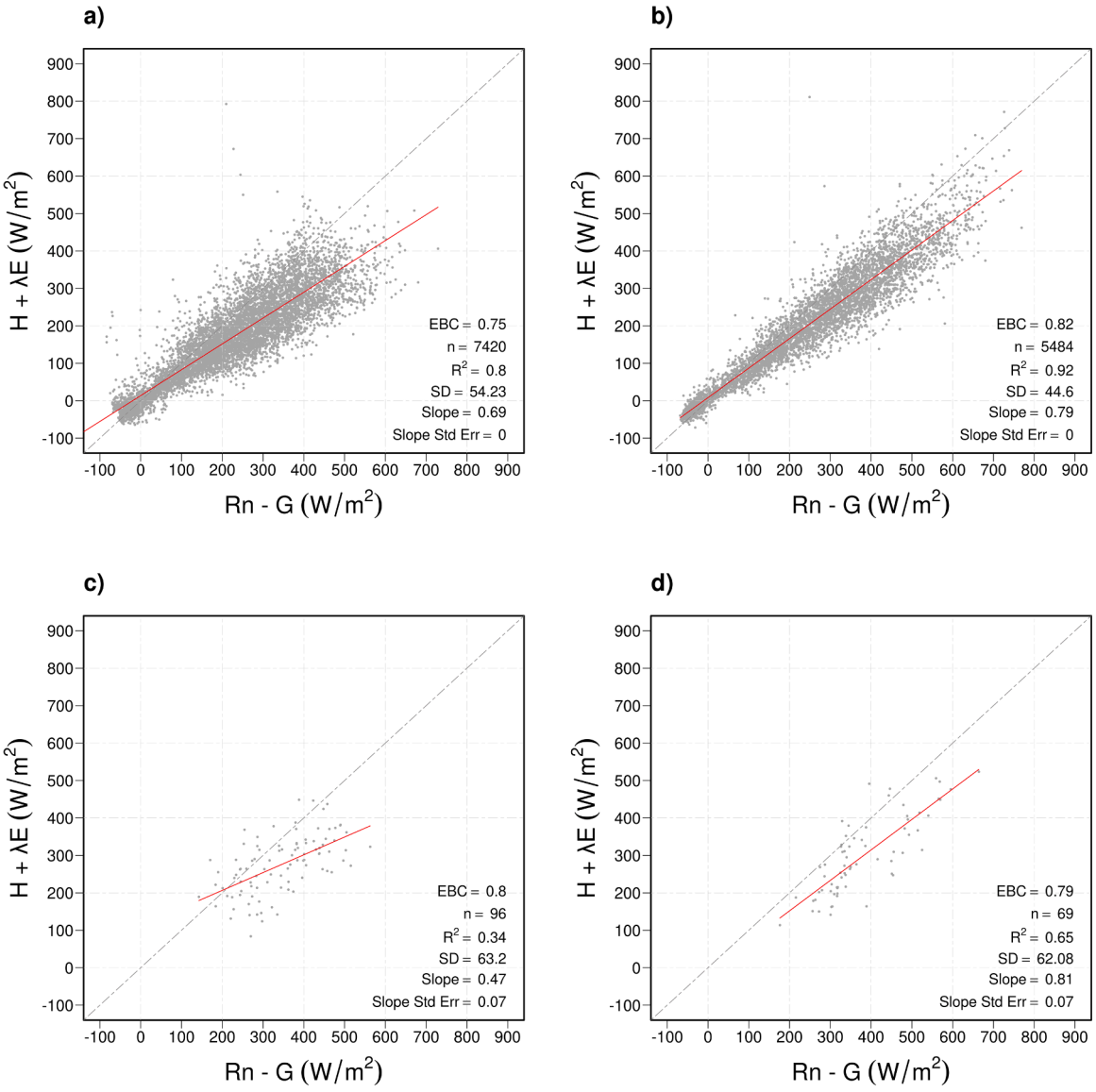

Fig. 4. Scatter-plots of the EC energy balance closure (net radiation minus soil heat flux ($R_n - G$) vs. sensible heat and latent heat fluxes ($H + \lambda E$)) for full study period on herbaceous-free (a) and herbaceous-cover (b), and for the days compared with the model on herbaceous-free (c) and herbaceous-cover (d). n (sample size), SD (standard deviation), EBC (EC Energy Balance Closure) $= \frac{\sum(H+\lambda E)}{\sum(R_n-G)}$

$$R_{n,C} \approx H_C + \lambda E_C \quad (3)$$

$$R_{n,S} \approx H_S + \lambda E_S + G \quad (4)$$

$$T_{rad}^4(\theta) = f_C(\theta)T_C^4 + [1 - f_C(\theta)]T_S^4 \quad (5)$$

where T is temperature, θ is the view zenith angle, f is the fraction of vegetation observed by the sensor (function of θ, LAI, and X_{LAD}) and suffixes $_S$ and $_C$ correspond to soil and canopy, respectively. H_S and H_C are calculated from the gradients between the aerodynamic temperature (T_0) and T_S and T_C, respectively. On the other hand, G is estimated according to Choudhury et al. (1987) as 35% of net soil radiation ($R_{n,S}$) (Norman et al., 1995).

As T_{rad} is obtained from a single observation angle, in order to partition fluxes, an initial estimation is required to determine T_S and T_C. For this, a first estimate of the canopy transpiration (λE_C, latent heat flux corresponding to the canopy) is given as

$$\lambda E_C = \alpha_{PT} f_g \frac{\Delta}{\Delta + \gamma} R_{n,C} \quad (6)$$

where $aPT \sim 1.26$ is the Priestley-Taylor coefficient, Δ is the slope of saturation vapour pressure curve at T_A and γ is the psychrometric constant. Thus, T_S and T_C are estimated in an iterative process in which it is assumed that only the photosynthetic active part of the canopy, expressed as f_g, transpires at a potential rate based on Priestley and Taylor (1972). Once this initial estimate of canopy transpiration is computed, T_S and T_C are estimated by inverting Eq. 3 and Eq. 5 and an initial estimate of λE_S is derived by inverting Eq. 4. If the computed $\lambda E_S <$ 0, which is non-physical solution for daytime convective conditions, it suggests the canopy is not transpiring at the potential rate, hence there is a sequential step-wise reduction of aPT, reducing λE_C, until realistic daytime fluxes for both λE_S and λE_C are computed, i.e. higher or equal to 0. Daily evapotranspiration (ET_d) is extrapolated according to Cammalleri et al. (2014) as a function of the ratio between TSEB estimated instantaneous λE_i and the instantaneous solar irradiance SI_i

$$ET_d = SI_d \frac{\lambda E_i}{SI_i} \quad (7)$$

where SI_d is daily solar irradiance. ET_d is transformed to mmd^{-1}

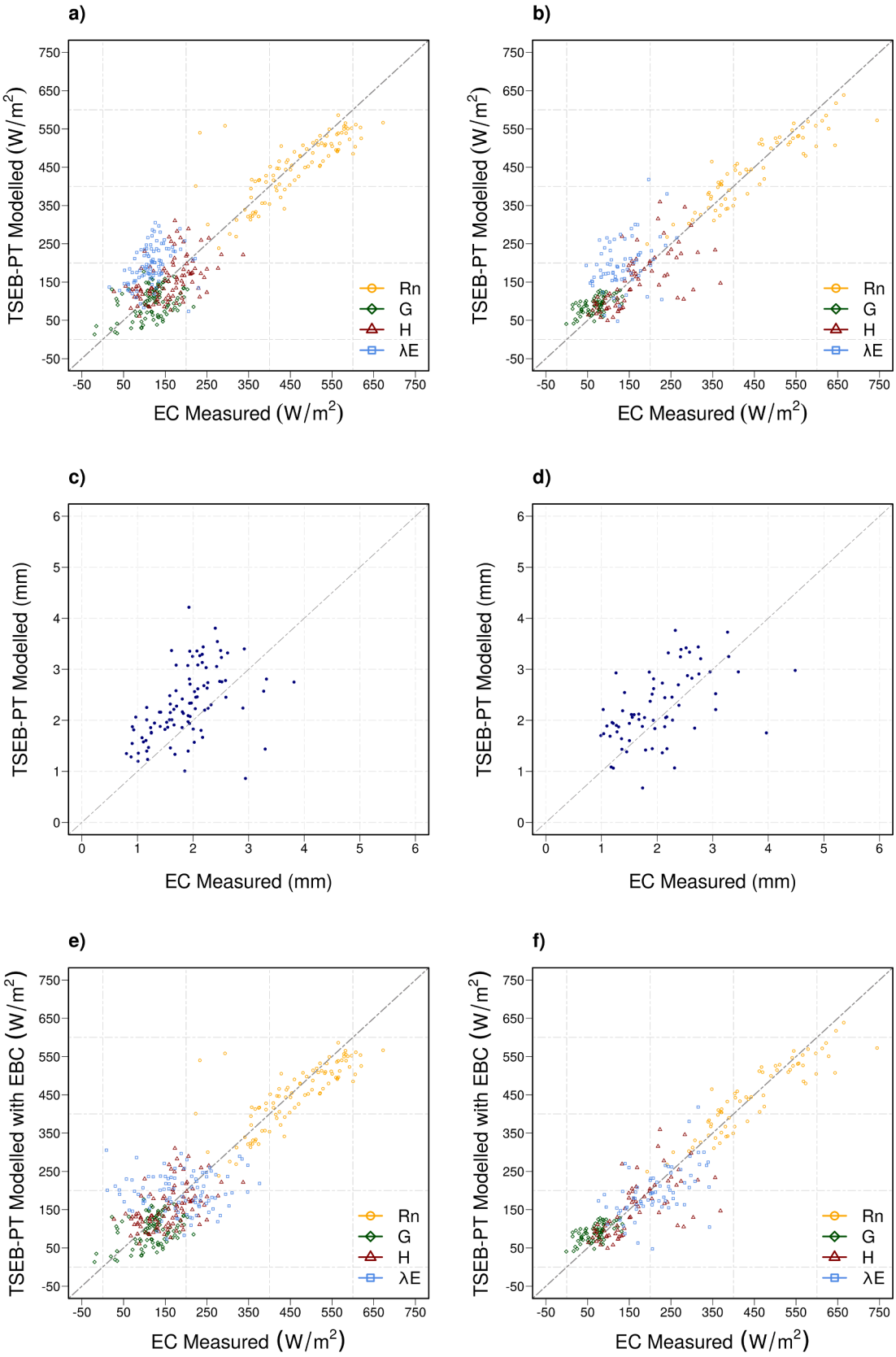

Fig. 5. Scatter-plots of the estimated values (TSEB-PT Model) vs. ground-based ones by eddy covariance (EC) measurements for the energy balance components on herbaceous-free (a) and herbaceous-cover (b), actual daily evapotranspiration on herbaceous-free (c) and herbaceous-cover (d) canopies, and the estimated values (TSEB-PT Model) with energy balance closure (EBC, by calculating λE as remainder of the energy balance) vs. ground-based ones by EC measurements for the energy balance components on herbaceous-free (e) and herbaceous-cover (f).

Table 2
Sample size (n), standard deviation (SD), mean bias (Bias), mean absolute difference (MAD), root mean square difference (RMSD) and Pearson correlation coefficient (r) between modelled values and EC measurements for net radiation (R_n), soil heat flux (G), sensible heat (H), latent heat (λE), latent heat with energy balance closure (λE (EBC)) and actual daily evapotranspiration (ET_d).

	Herbaceous-free Plot						Herbaceous-cover Plot					
Variable	n	SD (W/m^2)	Bias (W/m^2)	MAD (W/m^2)	RMSD (W/m^2)	r	n	SD (W/m^2)	Bias (W/m^2)	MAD (W/m^2)	RMSD (W/m^2)	r
R_n	96	62	-12	44	63	0.78	69	48	-5	38	48	0.91
G		48	-22	42	53	0.38		25	22	27	33	0.60
H		58	-3	47	57	0.47		63	-13	44	64	0.66
λE		50	78	83	93	0.36		65	64	76	91	0.38
λE (EBC)		92	9	75	92	0.04		64	-17	49	66	0.54
		SD (mm)	Bias (mm)	MAD (mm)	RMSD (mm)			SD (mm)	Bias (mm)	MAD (mm)	RMSD (mm)	
ET_d		0.66	0.42	0.64	0.78	0.48		0.69	0.23	0.58	0.72	0.53

following Eq. 8,

$$ET_d = \frac{\lambda E}{\rho_w \lambda} 10^3 \ 24 \ 3600 \quad (8)$$

where ρ_w (kg·m^{-3}) is the density of air-free water at a pressure of 101.325 kPa, λ (J·kg^{-1}) is the latent heat of vaporization, λE is in W·m^{-2} and the conversion factors 10^3, 24 and 3600 are in mm·m^{-1}, h·d^{-1} and s·h^{-1}, respectively.

The modelled results (predicted) were compared to the ground-based measurements (observed), for the three year study. The Pearson correlation coefficient (r) and the residuals' standard deviation (SD) statistics were used as an indicator of scatter, whereas the Mean Absolute Difference (MAD) and Root Mean Square Difference (RMSD) (Chai and Draxler, 2014) were used to measure the differences between predicted and observed values; to quantify the model under- and over-estimations between predicted and observed values the mean Bias was computed, defined as the average of differences (predicted – observed).

3. Results

In total 771 S3 images were processed. After removing two outliers due to ground-based instrumentation errors, the total number of cloud-free images (i.e. days) with available ground-based measured flux data were 96 for HF (with 29, 6, 24, 37 during autumn, winter, spring and summer, respectively) and 69 for HC (with 24, 5, 19 and 21 for respective seasons).

Considering the plots' characteristics and homogeneity we assumed that the flow conditions are generally uniform for each plot. The criteria used for validation is illustrated in Fig. 3 for the October 11th 2016 scene. The output of the model for the selected pixels are compared with the ground-based obtained measurements. Thus, the modelled value for ET_d validation was obtained by averaging all the ET_d pixel values for each surface (panel "a"). The modelled pixel values selected for H and λE fluxes validation were the pixel where the peak of maximum influence of EC footprint is located at the satellite overpass time (dark blue dot on panel "b", example for the HF surface) which was weight averaged (50%) together with the adjacent pixels (50% remainder), following the footprint model described in Schmid (2002). The modelled pixel value selected for validate R_n and G was the fuchsia pixel (panel "c", example for the HF surface) which run into the pixels of both EC towers where the sensors for measuring these variables are installed.

In Fig. 4 the EC Energy Balance Closure (EBC) for the study area is shown. The EBC is 0.07 higher on HC than on HF for all the EC available measures throughout study period (panels "a" and "b"). Apart from, taking into account only the EC measurements compared with the model (panels "c" and "d"), EBC is 0.01 lower on the HC than on HF. However, for this specific reduced samples, while the slope on HC is similar to all the study period, on HF the slope and R^2 values are lower. Moreover, with respect to the available energy ($R_n - G$) the EC shows a mean underestimation fraction of the energy fluxes ($H + \lambda E$) of 0.25 and 0.18 on HF and HC respectively for all study period, and 0.20 and 0.21 respectively for only the modelled compared data.

Scatter-plots of predicted vs. observed data are shown in Fig. 5, and the validation metrics are shown in Table 2.

The model yields better agreement and greater correlations with the HC site. Nevertheless, the scatter for H and ET_d is very similar over both plots, whereas for λE there is greater scatter with HC compared to HF (SD difference of 15 W/m^2). In addition, the discrepancies are observed for both olive orchards at larger H values.

The model overestimates λE and ET_d on both types of surfaces, showing higher mean biases on HF than on HC (differences of 14 W/m^2 for λE and 0.19 mm for ET_d). Results with EBC (applied to the ground-based data by calculating λE as a remainder of the energy balance)

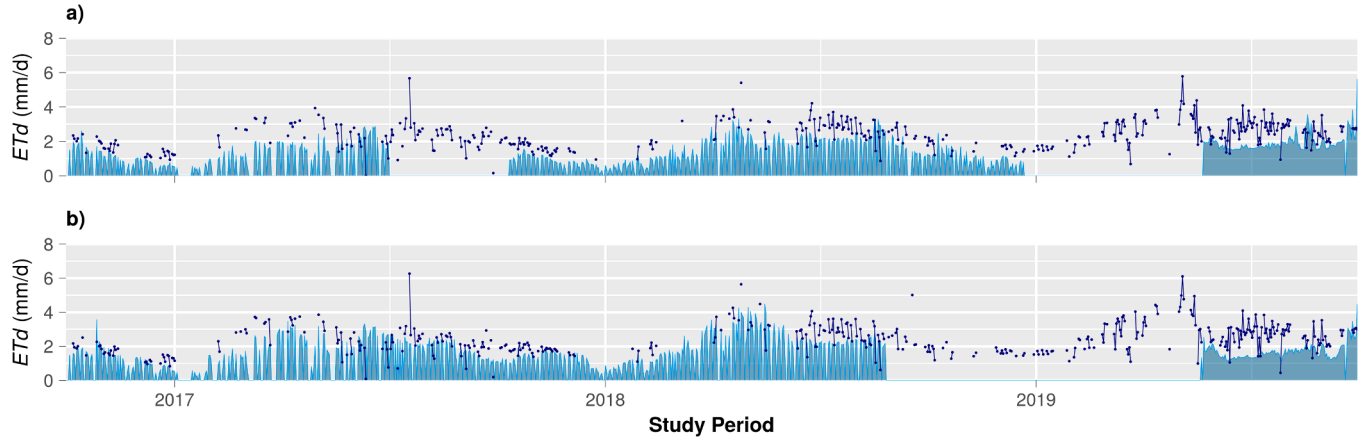

Fig. 6. Time series of daily evapotranspiration for herbaceous-free plot (a) and on herbaceous-cover plot (b). Shadow areas in light blue represent EC (in situ) measurements with uncorrected energy balance and dotted lines in dark blue represent the modelled values.

show better agreement overall. λE is neither significantly overestimated nor underestimated (although the difference of mean bias between orchards is 12 W/m^2 higher, the mean biases for both orchards are significantly lower). In contrast, R_n and H tends to be underestimated for both orchards (7 W/m^2 higher mean bias difference on HF for R_n and 10 W/m^2 higher on HC for H) but does not show important biases for R_n on HC and for H on HF. Instead, G is overestimated on HC and equally underestimated on HF, with a mean bias difference of 44 W/m^2 between both plots.

The values of MAD and RMSD between orchards are very similar for H (differences of 3 and 7 W/m^2, respectively), λE (7 and 2 W/m^2) and ET_d (0.06 mm for both metrics), while for R_n and G they are lower on HC than on HF (respective differences of 6 and 15 W/m^2 for R_n and 15 and 20 W/m^2 for G).

The Pearson correlation yielded higher values for ET_d than for λE, and very similar between both surfaces for these variables (differences of 0.05 and 0.02, respectively). It is higher for R_n and meaningfully higher for G and H on HC than on HF (differences of 0.13, 0.22 and 0.19, respectively).

Time series of ET_d for predicted and observed data on both orchards are shown in Fig. 6. Overall, both orchards show similar tendencies throughout the study period between them when compared against the measured values. Also, the magnitudes of ET_d are generally similar between orchards for both modelled values and EC in situ measurements, although a higher ET_d is observed for HC especially in spring periods, when the orchards are irrigated in the greatest productivity times (panel "b"). This is clearly seen in EC in situ measurements (shadow areas in light blue) whereas in the modelled values (dotted lines in dark blue), these differences are generally smaller.

4. Discussion

To our knowledge, this is the first study to assess, over three hydrological years (2016-2019) on herbaceous-cover and herbaceous-free surfaces in an irrigated olive orchard crop, the methodology proposed by Guzinski & Nieto (2019) to estimate actual evapotranspiration at high spatial and temporal resolutions by the TSEB model using Sentinel-2 and Sentinel-3 imagery. Guzinski and Nieto (2019) ran the TSEB model in barley fields and plantation conifer by few specific images from MODIS at 1 km spatial resolution for the LST, and from Landsat 5TM, 7ETM+ and 8OLI at 30 m for the VIS, NIR and resampled for TIR. Similarly, other studies have employed this methodology over other different surfaces and climate conditions. Thus, Bellvert et al. (2020) compared the TSEB with a water consumption crop model and stem water potential estimates for the growing season of 2018 in a vineyard. They did not have available EC data and worked with Sentinel imagery and airborne imagery at 0.25-m spatial resolution. Moreover, Guzinski et al. (2020) compared the TSEB, METRIC and ESVEP models using the Sentinel imagery (in which the combined S2-S3 scenes could reach 10 days) vs. EC measurements on eleven different canopies for 2017, amongst which a rain fed olive grove with 5-10% canopy cover was included. Other studies have also applied similar methods in olive orchard crops using few concrete images obtained by distinct remote sensing platforms and instruments. Table 3 summarises the mentioned studies together with the present one, showing the models, validation techniques and sites, as well as some characteristics of those sites, remote sensing platforms and sensors used together with some obtained results. Overall, the differences found in the present study are in agreement with those reported in previous studies.

The differences in R_n between orchards (HC and HF) and the better agreement showed for HC, could be explained by the differences between model footprint (20×20 m, with a homogeneous signal assumed) and in situ upwelling radiometer footprint sizes (< 20 m), as well as the different viewing angles between each radiometer (on HC and HF) and the satellite sensors. This, together with the fact that HC presents a higher f_C and more heterogeneity than on HF due to the additional herbs layer (not taken into account by the TSEB model), the specific orchards structure and geometry (with the natural growing and distribution of the herbaceous layer over the surface and throughout the study period), imply different perspectives and observed fractions of soil, herb, and trees by each radiometer on HC and HF, adding distinct uncertainties to the model agreements on each plot. Moreover, some R_n values in HF were corrected due to a small inclination of the 4-component radiometer, for which the incident radiation in HC vs. HF of short wave and long wave was used as reference.

The differences obtained for G compared to previous studies in Table 3 could be due to, on one hand, the constant fraction of $R_{n,S}$ we used to estimate G when the conditions affecting the relationship of this components probably were changing throughout the lengthy study period (Colaizzi et al., 2016b, 2016a; Norman et al., 1995; Santanello and Friedl, 2003). On the other hand, the used value for this purpose (0.35) might not be quite suitable for the study site, since this fraction might depend on the type of soil, latitude, and meteorological conditions (Choudhury et al., 1987). Consequently, this likely partially increased differences in the λE estimation. Additionally, the clear tendency to overestimate modelled G on HC reveals the model limitation on surfaces with additional layers (soil, herb, and trees canopy). This could be due to that part of R_n absorbed by the herbs understory before reaching the soil (Moderow et al., 2009) is not considered by a two-source model. As consequence, it could have resulted in a lower estimation of λE and, therefore, in a lower ET_d estimated on HC. Despite this, the results at the site were consistent with previous studies (Table 3). The smaller range and lowest differences obtained for G on HC in respect to HF might be due to the better adjusted parameterisation of f_C throughout the processed period, whereas on HF this parameter stayed constant. However, some herbs could have grown between herbicide treatments, suggesting that a more precise f_C parameterisation (adapted to the actual conditions at each moment) could partially compensate this model limitation and enhance its estimations. In contrast, the trend to underestimate G on HF supports the mentioned argument, where the use of a constant fraction of $R_{n,S}$ to calculate this component could not be quite suitable depending on the case.

It might be due to that EC errors in H increase with the magnitude of H, or it might suggest a decrease in the methodology's accuracy at higher values of H. In this last case, because H is directly related to LST and its estimation depending on T_A and wind speed (Norman et al., 1995), two possible reasons could have influenced this difference and the better agreement obtained by Hoedjes et al. (2008) for this component: (1) the use of higher spatial resolution for TIR range (i.e. without applying any sharpening process) as well as (2) local meteorological forcing. On one hand, the used methodology is firstly based in a sharpening process of T_{rad} from 1 km to 20 m spatial resolution that, through statistical relationships between TIR and VIS/NIR datasets, estimates the LST at 20 m. Guzinski et al. (2020) discussed that H is the energy balance component most prone to error in that process, and in this sense, Bellvert et al. (2020) reported a tendency to underestimate the LST in extreme dry conditions probably caused by the fact that at 1 km scale is not possible to reflect all dynamic range of surface temperatures occurring at field scale. As shown in Fig. 7, although the sharpened LST showed a good agreement and explained correctly the temporal trends, there is a tendency to overestimate the LST which increases when its values increase. This could be due to the previously mentioned surface characteristics and the differences in the footprints of the model and the in situ radiometers, as well as the soil and type of canopy observed fractions by each one. This would imply a more homogeneous sharpened LST at 20 m model footprint (more balanced fractions of soil, herb, and trees), and in situ lower LST (calculated from the radiometers measures according to Burchard-Levine et al., 2020) where the radiometer footprint could have observed a higher canopy fraction (lower LST) than the satellite sensor at model spatial resolution. On the other hand, the coarse spatial resolution of non-local meteorological data used for this study (ECMWF ERA5 reanalysis data set),

Table 3
Comparative summary of studies. Sample size (n), mean bias (Bias, W/m^2), mean absolute difference (MAD, W/m^2), root mean square difference (RMSD, W/m^2) and Pearson correlation coefficient (r, dimensionless) between modelled and observed (VS.) values for net radiation (R_n), soil heat flux (G), sensible heat (H), latent heat flux (λE), and actual daily evapotranspiration (ET_d, mm). TSEB (Two Source Energy Balance), PT (Priestly-Taylor), DMS (Data Mining Sharpening), SW (Shuttleworth-Walace), SSEBop (Operational Simplified Surface Energy Balance), DLST (Disaggregated Land Surface Temperature), RSEB (Remote Sensing Energy Balance), METRIC (Mapping Evapotranspiration at high Resolution with Internalised Calibration), FAO-56 (standardised crop evapotranspiration (Allen et al. (1998)), K_C (tabled basal crop coefficients), PM (Penman-Monteith), app. (approach), AE (Available Energy), EF (Evaporative Fraction), S2 (Sentinel-2), S3 (Sentinel-3), VIS (Visible range), NIR (Near Infrared range), TIR (Thermal Infrared range), LST (Land Surface Temperature), NDVI (Normalized Difference Vegetation Index), EC (Eddy Covariance), ECMWF (European Centre for Medium-Range Weather Forecasts), 2T (directly differentiated soil and canopy temperatures at high spatial resolution), Meteo-Data (Meteorological Data), SAS (Small Aperture Scintillometer). *To be able to directly compare the results with Pôças (2014) we have calculated the Bias, MADs and RMSDs for this study from their published data.

Study	Model Used	Remote Sensing	VS.	Site	n	R_n				G	
						Bias	MAD	RMSD	r	Bias	MAD
Hoedjes (2008)	Based on AE and EF	Terra/Aster (15/30 m VIS/NIR 90 m TIR)	EC, Local Meteo-Data and TIR sensors	Olive orchard (Semi-arid Morocco) (Flood-Irrigated)	6	RMSD of AE ($R_n - G$) = 51 Wm^{-2}					
Cammarelli (2010)	TSEB (Goudriaan)	Airborne (0.6 m VIS/NIR 1.7 m TIR aggregated at 12 m)	EC and Local SAS Micro-Meteo-Data	Olive Orchard (Sicily) (Drip-Irrigated)	7		23	28			15
	TSEB (Massman)										14
	TSEB (Lalic)							29			15
Cammarelli (2013)	Modified FAO-56 (K_c) Modified FAO-56 (PM)	Airborne (0.6 m VIS/NIR 1.7 m TIR)	EC, Sap flow and Micro-Meteo-Data								
Pôças (2014)*	METRIC	Landsat 5/7 (30 m VIS/NIR 120/60 m TIR)	EC, Sap Flow and Microlysimeters	Olive orchard Super Intensive (South Portugal) (Drip-Irrigated)	15						
Paço (2014)			Sap flow and Microlysimeters								
Ortega-Farías (2016)	RSEB	Airborne (0.06 m TIR)	EC	Olive orchard (Center Chile) (Drip-Irrigated)	10			38			
Olivera-Guerra (2017)	SSEBop (DLST) SSEBop (Landsat 8)	Landsat 8 (30 m VIS/NIR/TIR) MODIS LST/NDVI (1 km / 250 m)	Meteo-Data	Olive orchard (Atacama, Chile)	21-25						
This with λE (EBC)	TSEB-PT (DMS)	S2/S3 (10/20/60 m VIS/NIR 1 km TIR)	EC, Meteo-Data and ECMWF ERA5 Reanalysis	**Olive orchard (Herbaceous-free, South-East Spain)**	**96**	**-12**	**44**	**63**	**0.78**	**-22**	**42**
				Olive orchard (Herbaceous-cover, South-East Spain)	**69**	**-5**	**38**	**48**	**0.91**	**22**	**27**
Guzinski (2020)			EC and ECMWF ERA5 Reanalysis	All 11 sites	≈482	-14	44	56	0.91	14	44
				Croplands	≈204	-10	32	42	0.95	46	56
				Herbaceous crops	≈65	-36	40	47	0.98	34	55
				Woody crops	≈138	1	29	40	0.95	51	57
				Semi-arid climate	≈383	-11	47	59	0.88	11	44
				Temperate climate	≈99	-23	35	43	0.98	26	43
Bellvert (2020)			TSEB-PT (HR-Airborne) TSEB-2T (HR-Airborne)	Vineyard (North-East Spain)	3						
Guzinski & Nieto (2019)		Landsat 5/7/8 (30 m VIS/NIR 120/60/30 m TIR) MODIS LST (1 km)	EC Measurms.	Barley fields (Denmark)	19	-16		29	0.98	-2	
				Conifer Plantation Forest (Denmark)		-27			1.00	3	

might also add uncertainty with respect to local meteorological data (Guzinski et al., 2020). In this sense, the ERA5 reanalysis used data versus in situ measurements are shown in Fig.s 8, 9 and 10. Wind speed shows a high variation and worse fit when compared with shortwave irradiance and T_A. Shortwave irradiance shows an overestimation for both orchards with an averaged SD between them of 57 W/m^2. T_A shows a low variation and the best fit with a SD around 1.3 °C (~ 48% lower than LST).

Evident reasons for the overestimates of λE and ET_d are the previously mentioned ones, which provide uncertainties in the estimated energy balance components, since λE is obtained as residual term. An additional possible reason for the observed overestimations in λE and as consequence in ET_d could be the limitations of the EC measurements used to validate the fluxes. The imbalanced energy components by the EC technique (Fig. 4) is a well-known issue in the scientific community (e.g. Foken et al., 2011) that might contribute to such overestimation. Thus, the EC underestimations of H and λE might partially explain the lower correlations and higher differences versus studies which used different validation methods.

Results with EBC show better agreement overall compared to the results without EBC. However, the higher uncertainties obtained by the model on HF versus HC for R_n (probably influenced by the R_n correction

G		*H*				*λE*				ET_d			
RMSD	r	Bias	MAD	RMSD	r	Bias	MAD	RMSD	r	Bias	MAD	RMSD	r
RMSD of AE ($R_n - G$) = 51 Wm^{-2}				27				48					
17			32	40			37	43					
16			25	32			34	40					
17			89	92			96	98					
											≈ 0.53-0.59	≈ 0.66-0.80	
											≈ 0.48	≈ 0.61	
										0.34		0.60	
											0.4-0.6		
19				56				50					
										0.41		0.50	
										0.27		0.49	
53	**0.38**	**-3**	**47**	**57**	**0.47**	**9**	**75**	**92**	**0.04**	**0.42**	**0.64**	**0.78**	**0.48**
33	**0.60**	**-13**	**44**	**64**	**0.66**	**-17**	**49**	**66**	**0.54**	**0.23**	**0.58**	**0.72**	**0.53**
54	0.45	-47	65	81	0.67	22	72	89	0.76				
646464	0.25	-57	71	86	0.50	11	67	82	0.75				
	0.30	-39	55	71	0.51	-42	78	93	0.66				
	0.47	-67	80	94	0.52	36	61	76	0.84				
54	0.40	-51	69	84	0.68	32	71	86	0.76				
55	0.40	-32	53	71	0.64	-19	79	99	0.74				
												0.62	
												1.35	
31	0.40	11		60	0.66	-20		58	0.73				
11	0.11	-19		74	0.75	-48		90	0.62				

realized in some EC data on HF) and *G* influence in the small (MAD) or null (RMSD) differences reduction, and in the decrease of the Pearson correlation coefficient in this orchard with respect to the results without applying EBC compared to the obtained ones on HC when the EBC is applied.

Additionally, the better results on HC versus HF in the EBC imbalance between the compared days with the model on each orchard (Fig. 4, panels c and d), might also partially explain the better results obtained by the model on HC in each case (with and without EBC), when the contrary would be expected.

Also, the spatial variability in the model estimation of ET_d could partially explain the differences between observed vs. estimated ET_d, considering that each modelled ET_d value was estimated by averaging all the pixels contained in a given image (satellite overpass) for each plot, whereas the observed value (used as reference) corresponds to few EC footprint pixels at a certain instant throughout the day.

The observed LST values very close to 0 (Fig. 7) are related to images with some sparse clouds over the study area that were not properly detected by the Sen2Cor cloud mask and got included in the process and analysis. They were wrongly estimated and consequently affected the agreements in results. However, as this study aimed to test the operational capabilities of Sentinel imagery to estimate water fluxes in olive

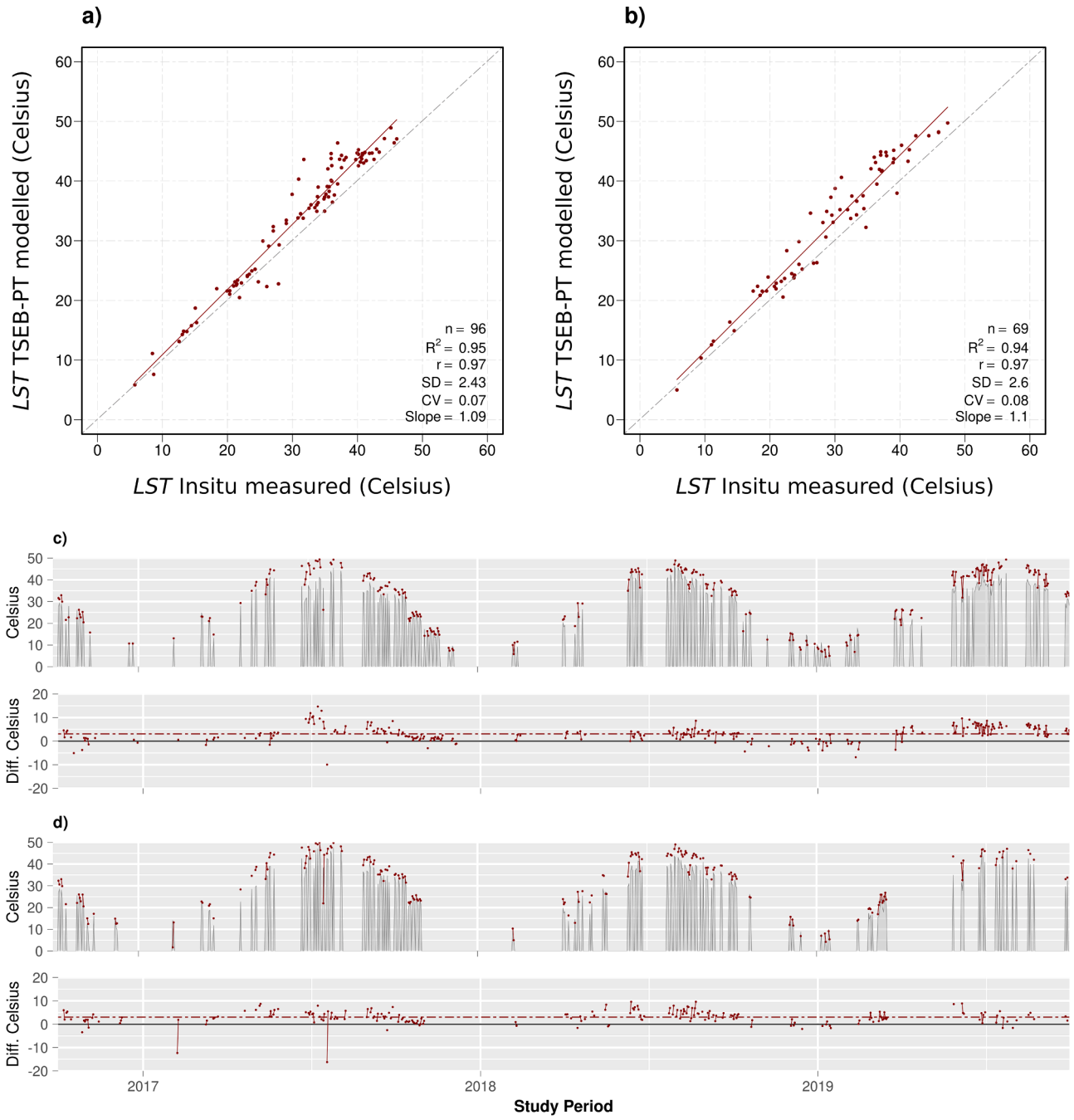

Fig. 7. Land Surface Temperature (LST) (Celsius degrees). In situ measurements vs. used ones by model on herbaceous-free plot (a) and on herbaceous-cover plot (b). Time series for full study period and its differences on herbaceous-free plot (c) and on herbaceous-cover plot (d). Shadow areas represents in situ measurements and colour dot-lines represents the values used by model. n (sample size), R^2 (determination coefficient), r (Pearson correlation coefficient), SD (standard deviation) and CV (variation coefficient).

orchards, these few outliers were kept in the validation dataset.

5. Conclusions

The proposed methodology to estimate ET_d can be directly and systematically applied without any calibration process and using only open public data and software. It resulted in high spatial resolution distributed ET_d estimates which were shown to be consistent with literature and acceptable for some farming activities in olive orchards. Furthermore, the high number of processed and analysed images, as well as the heterogeneity of the surfaces and the period studied, provide consistency to the results. These features show that this methodology is robust

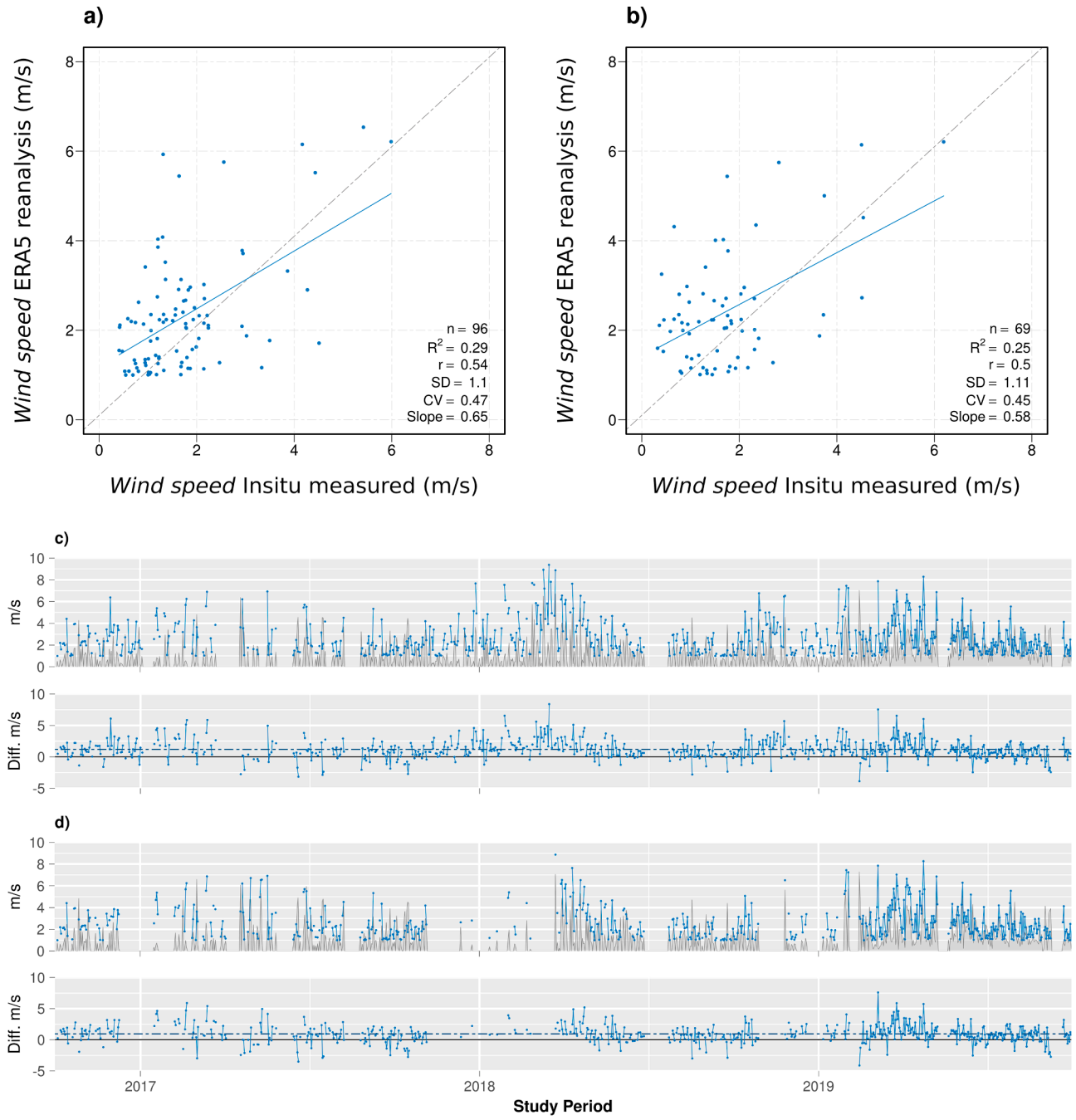

Fig. 8. Wind speed (m/s). In situ measurements vs. used ones by model on herbaceous-free plot (a) and on herbaceous-cover plot (b). Time series for full study period and its differences on herbaceous-free plot (c) and on herbaceous-cover plot (d). Shadow areas represents in situ measurements and colour dot-lines represents the values used by model. n (sample size), R^2 (determination coefficient), r (Pearson correlation coefficient), SD (standard deviation) and CV (variation coefficient).

and useful, until a high-spatial resolution high-revisit time thermal mission is launched, for long-term periods according to the Sentinel missions, which are expected operatives for the next decades. However, due to this systematic application it is possible to find issues in environmental and atmospheric conditions (e.g. ice or snow on surface), as well as in the quality of images and input data (e.g. cloud shadows or cloudy areas not properly detected by the masks) that could limit the results. Similarly to other studies, we consider that model accuracy

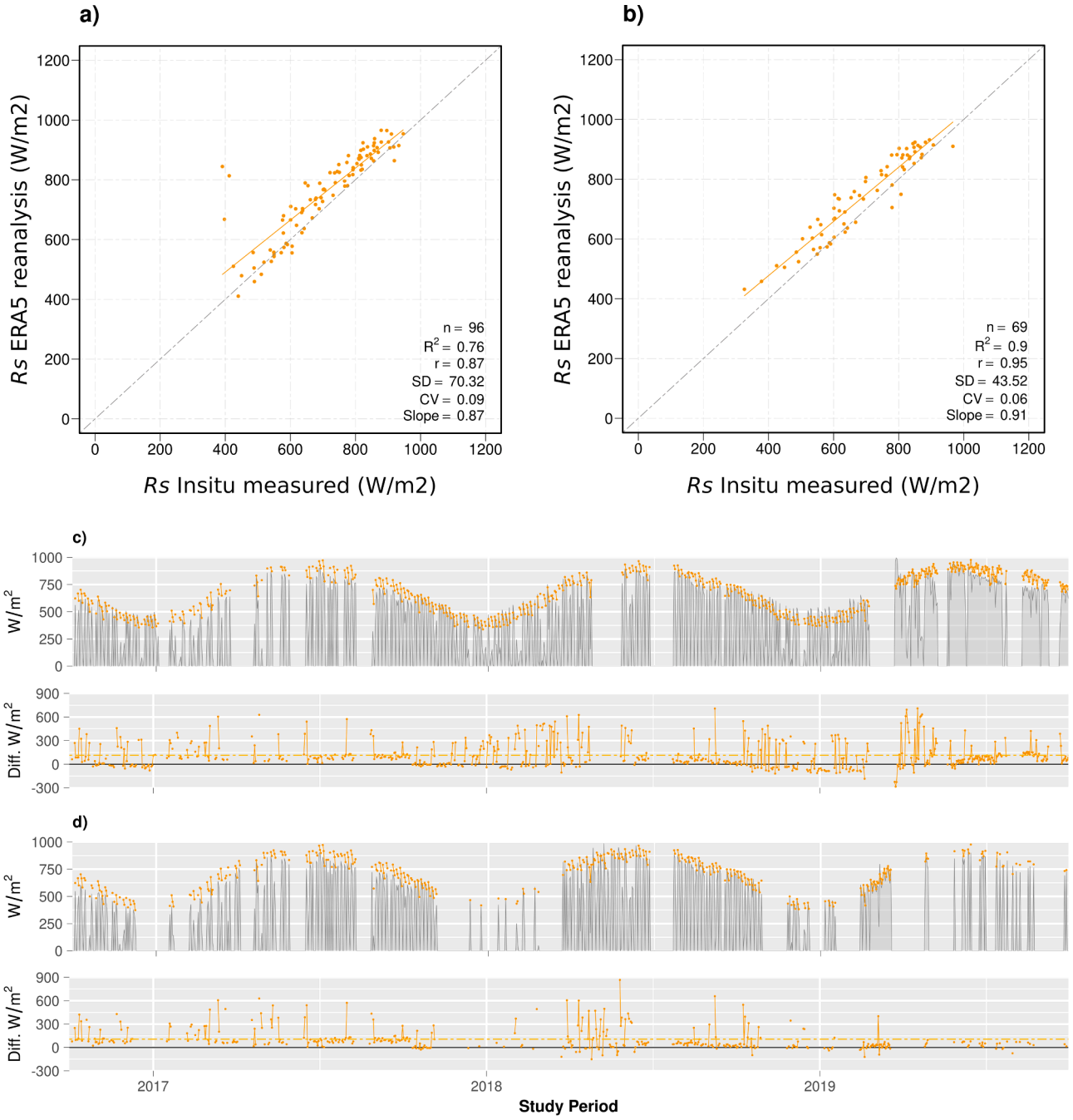

Fig. 9. Shortwave irradiance (R_S, W/m^2). In situ measurements vs. used ones by model on herbaceous-free plot (a) and on herbaceous-cover plot (b). Time series for full study period and its differences on herbaceous-free plot (c) and on herbaceous-cover plot (d). Shadow areas represents in situ measurements and colour dot-lines represents the values used by model. n (sample size), R^2 (determination coefficient), r (Pearson correlation coefficient), SD (standard deviation) and CV (variation coefficient).

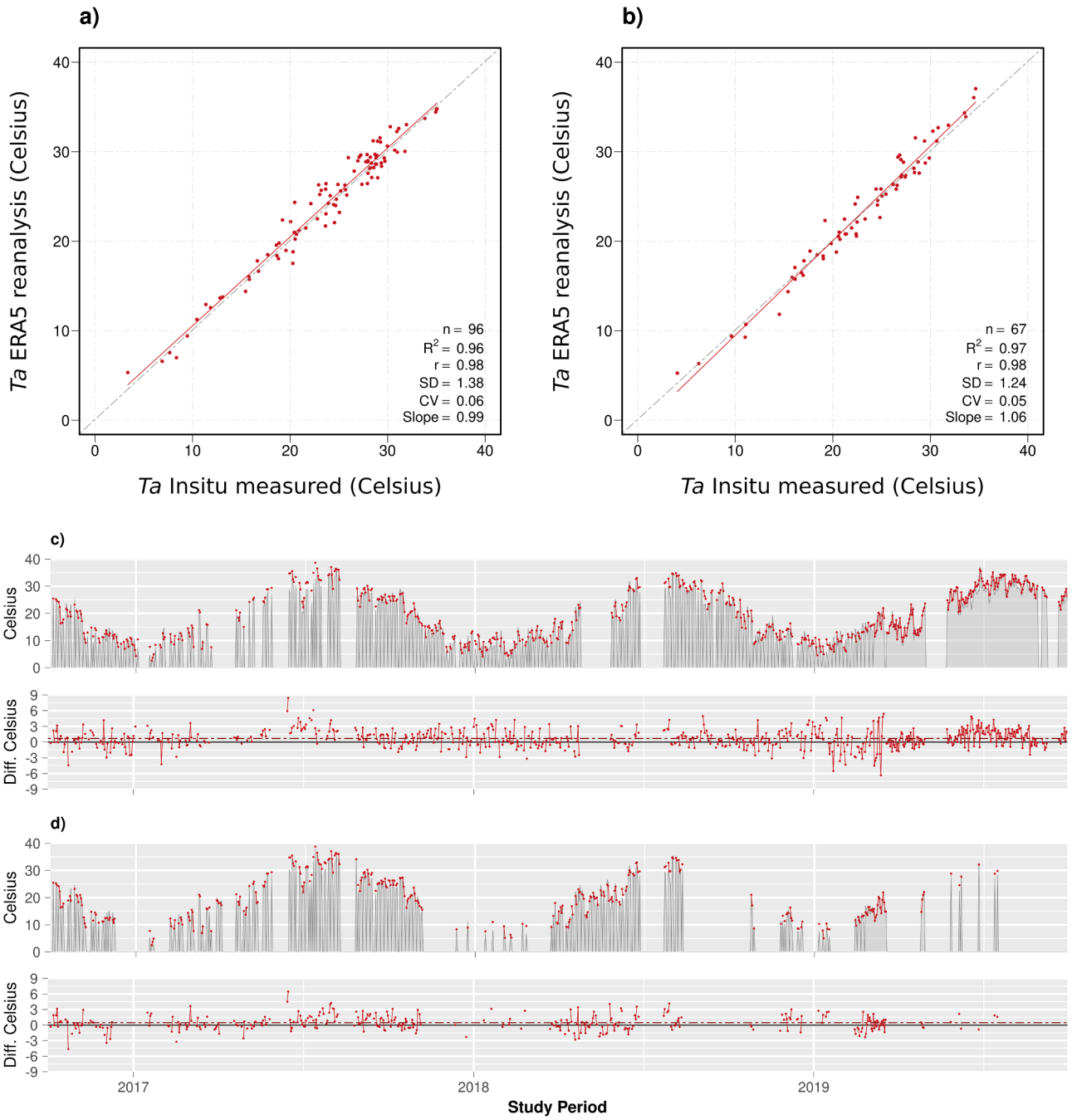

Fig. 10. Air Temperature (T_A) (Celsius degrees). In situ measurements vs. used ones by model on herbaceous-free plot (a) and on herbaceous-cover plot (b). Time series for full study period and its differences on herbaceous-free plot (c) and on herbaceous-cover plot (d). Shadow areas represents in situ measurements and colour dot-lines represents the values used by model. n (sample size), R^2 (determination coefficient), r (Pearson correlation coefficient), SD (standard deviation) and CV (variation coefficient).

could improve by using local meteorological data (especially wind speed measurements) as well as using a finer and more suitable spatial resolution of TIR data according to the surface and crop characteristics to enhance the LST and H estimations. A public satellite mission that combines high spatial and temporal resolutions in the TIR range would be desirable. Likewise, an accurate f_C and canopy height parameterisation adapted to the site and actual conditions at each moment is an important factor to obtain better estimations.

Moreover, model accuracy in estimating G could be improved by parameterising the R_n fraction and taking into account the soil type and state, as well as the diurnal variation of G with respect to R_n according to site latitude and day of year.

On the other hand, the limitation of the EC energy flux imbalance versus available energy, as a validation method contributed to greater disagreement of the model. Even so, the results showed no unreasonable differences in comparison with the literature. In this regard, the particular features of the EC samples that could be compared in each plot had an important influence in the agreement found between them and the EC measures. Hence, combining different validation techniques and methods in the future might help to better understand the model working and improve its accuracy.

Declaration of Competing Interest

The authors declare the following financial interests/personal relationships which may be considered as potential competing interests:

Sergio-David Aguirre-Garcia reports financial support was provided by Spanish Ministry of Science and Innovation, Project CGL2017-83538-C3-1-R, Grant number PRE2018-085638.

Acknowledgments

To the European Space Agency for the imagery of the Sentinel Missions and its open access. Special thanks to Radoslaw Guzinski for share and make accessible (https://github.com/radosuav/pyDMS) the implemented software for the used sharpening process (likewise to Hector Nieto for the implemented TSEB-PT, https://github.com/hectornieto/pyTSEB). To the Group of Castillo de Canena for the use of their farm as an experimental site and their people for continuous cooperation. We also give special thanks to Andrew S. Kowalski for his advice and suggestions. We would like also to express our gratitude to the anonymous reviewers for their comments and suggestions that enhanced this work. This work was supported by the Spanish Ministry of Science and Innovation through project CGL2017-83538-C3-1-R (ELEMENTAL) and PID2020-117825GB-C21 (INTEGRATYON^3) Including European Union ERDF funds [grant number PRE2018-085638]. Funding for open access charge: Universidad de Granada / CBUA.

References

Allen, R.G., Pereira, L.S., Raes, D., Smith, M., (1998). Crop evapotranspiration - Guidelines for computing crop water requirements - FAO Irrigation and drainage paper n. 56, Rome, Italy, 326pp.

Bellvert, J., Jofre-Ĉekalović, C., Pelechá, A., Mata, M., Nieto, H., 2020. Feasibility of using the two-source energy balance model (TSEB) with Sentinel-2 and Sentinel-3 images to analyze the spatio-temporal variability of vine water status in a vineyard. Remote Sens. 12 https://doi.org/10.3390/rs12142299.

Bisquert, M., Sánchez, J.M., López-Urrea, R., Caselles, V., 2016. Estimating high resolution evapotranspiration from disaggregated thermal images. Remote Sens. Environ. 187, 423–433. https://doi.org/10.1016/j.rse.2016.10.049.

Burchard-Levine, V., Nieto, H., Riaño, D., Migliavacca, M., El-Madany, T.S., Perez-Priego, O., Carrara, A., Martín, M.P., 2020. Seasonal adaptation of the thermal-based two-source energy balance model for estimating evapotranspiration in a semiarid tree-grass ecosystem. Remote Sens. 12, 904. https://doi.org/10.3390/rs12060904.

Cammalleri, C., Anderson, M.C., Ciraolo, G., Durso, G., Kustas, W.P., Loggia, G., La, Minacapilli, M., 2010. The impact of in-canopy wind profile formulations on heat flux estimation in an open orchard using the remote sensing-based two-source model. Hydrol. Earth Syst. Sci. 14, 2643–2659. https://doi.org/10.5194/hess-14-2643-2010.

Cammalleri, C., Anderson, M.C., Kustas, W.P., 2014. Upscaling of evapotranspiration fluxes from instantaneous to daytime scales for thermal remote sensing applications. Hydrol. Earth Syst. Sci. 18, 1885–1894. https://doi.org/10.5194/hess-18-1885-2014.

Cammalleri, C., Ciraolo, G., Minacapilli, M., Rallo, G., 2013. Evapotranspiration from an olive orchard using remote sensing-based dual crop coefficient approach. Water Resour. Manag. 27, 4877–4895. https://doi.org/10.1007/s11269-013-0444-7.

Campbell, G.S., Norman, J.M., 1998. An Introduction to Environmental Biophysics, 2nd ed. Springer, New York, New York, NY. https://doi.org/10.1007/978-1-4612-1626-1.

Carpintero, E., Andreu, A., Gómez-Giráldez, P.J., Blázquez, Á., González-Dugo, M.P., 2020. Remote-sensing-based water balance for monitoring of evapotranspiration and water stress of a mediterranean Oak-Grass Savanna. Water (Switzerland) 12, 1418. https://doi.org/10.3390/w12051418.

Chai, T., Draxler, R.R., 2014. Root mean square error (RMSE) or mean absolute error (MAE)? – Arguments against avoiding RMSE in the literature. Geosci. Model Dev. 7, 1247–1250. https://doi.org/10.5194/gmd-7-1247-2014.

Chamizo, S., Serrano-Ortiz, P., López-Ballesteros, A., Sánchez-Cañete, E.P., Vicente-Vicente, J.L., Kowalski, A.S., 2017. Net ecosystem CO2exchange in an irrigated olive orchard of SE Spain: Influence of weed cover. Agric. Ecosyst. Environ. 239, 51–64. https://doi.org/10.1016/j.agee.2017.01.016.

Chen, X., Li, W., Chen, J., Rao, Y., Yamaguchi, Y., 2014. A combination of TsHARP and thin plate spline interpolation for spatial sharpening of thermal imagery. Remote Sens 6, 2845–2863. https://doi.org/10.3390/rs6042845.

Choudhury, B.J., Idso, S.B., Reginato, R.J., 1987. Analysis of an empirical model for soil heat flux under a growing wheat crop for estimating evaporation by an infrared-temperature based energy balance equation. Agric. For. Meteorol. 39, 283–297. https://doi.org/10.1016/0168-1923(87)90021-9.

Colaizzi, P.D., Evett, S.R., Agam, N., Schwartz, R.C., Kustas, W.P., 2016a. Soil heat flux calculation for sunlit and shaded surfaces under row crops: 1. Model development and sensitivity analysis. Agric. For. Meteorol. 216, 115–128. https://doi.org/10.1016/J.AGRFORMET.2015.10.010.

Colaizzi, P.D., Evett, S.R., Agam, N., Schwartz, R.C., Kustas, W.P., Cosh, M.H., McKee, L., 2016b. Soil heat flux calculation for sunlit and shaded surfaces under row crops: 2. Model test. Agric. For. Meteorol. 216, 129–140. https://doi.org/10.1016/J.AGRFORMET.2015.10.009.

Courault, D., Seguin, B., Olioso, A., 2005. Review on estimation of evapotranspiration from remote sensing data: From empirical to numerical modeling approaches. Irrig. Drain. Syst. 19, 223–249. https://doi.org/10.1007/s10795-005-5186-0.

Dabberdt, W. F., Lenschow, D. H., Horst, T. W., Zimmerman, P. R., Oncley, S. P., … Delany, A. C. (1993). Atmosphere-Surface Exchange Measurements. Science, 260 (5113), 14721481. https://doi.org/10.1126/science.260.5113.1472.

Donlon, C., Berruti, B., Buongiorno, A., Ferreira, M.H., Féménias, P., Frerick, J., Goryl, P., Klein, U., Laur, H., Mavrocordatos, C., Nieke, J., Rebhan, H., Seitz, B., Stroede, J., Sciarra, R., 2012. The global monitoring for environment and security (GMES) sentinel-3 mission. Remote Sens. Environ. 120, 37–57. https://doi.org/10.1016/j.rse.2011.07.024.

Drusch, M., Del Bello, U., Carlier, S., Colin, O., Fernandez, V., Gascon, F., Hoersch, B., Isola, C., Laberinti, P., Martimort, P., Meygret, A., Spoto, F., Sy, O., Marchese, F., Bargellini, P., 2012. Sentinel-2: ESA's optical high-resolution mission for GMES operational services. Remote Sens. Environ. 120, 25–36. https://doi.org/10.1016/j.rse.2011.11.026.

Féret, J.B., Gitelson, A.A., Noble, S.D., Jacquemoud, S., 2017. PROSPECT-D: towards modeling leaf optical properties through a complete lifecycle. Remote Sens. Environ. 193, 204–215. https://doi.org/10.1016/j.rse.2017.03.004.

Fisher, J.B., Tu, K.P., Baldocchi, D.D., 2008. Global estimates of the land-atmosphere water flux based on monthly AVHRR and ISLSCP-II data, validated at 16 FLUXNET sites. Remote Sens. Environ. 112, 901–919. https://doi.org/10.1016/j.rse.2007.06.025.

Foken, T., Aubinet, M., Finnigan, J.J., Leclerc, M.Y., Mauder, M., Paw, U, K.T., 2011. Results of a panel discussion about the energy balance closure correction for trace gases. Bull. Am. Meteorol. Soc. 92, 13–18. https://doi.org/10.1175/2011BAMS3130.1.

French, A.N., Hunsaker, D.J., Sanchez, C.A., Saber, M., Gonzalez, J.R., Anderson, R., 2020. Satellite-based NDVI crop coefficients and evapotranspiration with eddy covariance validation for multiple durum wheat fields in the US Southwest. Agric. Water Manag. 239, 106266 https://doi.org/10.1016/j.agwat.2020.106266.

Fuentes-Peñailillo, F., Ortega-Farías, S., Acevedo-Opazo, C., Fonseca-Luengo, D., 2018. Implementation of a two-source model for estimating the spatial variability of olive evapotranspiration using satellite images and ground-based climate data. Water (Switzerland) 10. https://doi.org/10.3390/w10030339.

Gao, F., Kustas, W., Anderson, M., 2012. A data mining approach for sharpening thermal satellite imagery over land. Remote Sens. 4, 3287–3319. https://doi.org/10.3390/rs4113287.

García-Valdecasas Ojeda, M., Rosa-Cánovas, J.J., Romero-Jiménez, E., Yeste, P., Gámiz-Fortis, S.R., Castro-Díez, Y., Esteban-Parra, M.J., 2020. The role of the surface evapotranspiration in regional climate modelling: evaluation and near-term future changes. Atmos. Res. 237, 104867 https://doi.org/10.1016/j.atmosres.2020.104867.

García, M., Sandholt, I., Ceccato, P., Ridler, M., Mougin, E., Kergoat, L., Morillas, L., Timouk, F., Fensholt, R., Domingo, F., 2013. Actual evapotranspiration in drylands derived from in-situ and satellite data: assessing biophysical constraints. Remote Sens. Environ. 131, 103–118. https://doi.org/10.1016/j.rse.2012.12.016.

Gatti, A., Galoppo, A., Castellani, C., Carriero, F., 2018. Sentinel-2 Products Specification Document. Thales Alenia Space.

Gavilán, V., Lillo-Saavedra, M., Holzapfel, E., Rivera, D., García-Pedrero, A., 2019. Seasonal crop water balance using harmonized Landsat-8 and Sentinel-2 time series data. Water (Switzerland) 11, 2236. https://doi.org/10.3390/w11112236.

Guzinski, R., Anderson, M.C., Kustas, W.P., Nieto, H., Sandholt, I., 2013. Using a thermal-based two source energy balance model with time-differencing to estimate surface energy fluxes with day-night MODIS observations. Hydrol. Earth Syst. Sci. 17, 2809–2825. https://doi.org/10.5194/hess-17-2809-2013.

Guzinski, R., Nieto, H., 2019. Evaluating the feasibility of using sentinel-2 and sentinel-3 satellites for high-resolution evapotranspiration estimations. Remote Sens. Environ. 221, 157–172. https://doi.org/10.1016/j.rse.2018.11.019.

Guzinski, R., Nieto, H., Sandholt, I., Karamitilios, G., 2020. Modelling high-resolution actual evapotranspiration through Sentinel-2 and Sentinel-3 data fusion. Remote Sens 12. https://doi.org/10.3390/RS12091433.

Häusler, M., Conceição, N., Tezza, L., Sánchez, J.M., Campagnolo, M.L., Häusler, A.J., Silva, J.M.N., Warneke, T., Heygster, G., Ferreira, M.I., 2018. Estimation and partitioning of actual daily evapotranspiration at an intensive olive grove using the STSEB model based on remote sensing. Agric. Water Manag. 201, 188–198. https://doi.org/10.1016/j.agwat.2018.01.027.

Hoedjes, J.C.B., Chehbouni, A., Jacob, F., Ezzahar, J., Boulet, G., 2008. Deriving daily evapotranspiration from remotely sensed instantaneous evaporative fraction over olive orchard in semi-arid Morocco. J. Hydrol. 354, 53–64. https://doi.org/10.1016/j.jhydrol.2008.02.016.

Jaafar, H.H., Ahmad, F.A., 2020. Time series trends of Landsat-based ET using automated calibration in METRIC and SEBAL: The Bekaa Valley. Lebanon. Remote Sens. Environ. 238, 111034 https://doi.org/10.1016/j.rse.2018.12.033.

Kalma, J.D., McVicar, T.R., McCabe, M.F., 2008. Estimating land surface evaporation: A review of methods using remotely sensed surface temperature data. Surv. Geophys. 29, 421–469. https://doi.org/10.1007/s10712-008-9037-z.

Kappelle, M., Nations, U., Programme, E., 2020. WMO Statement on the State of the Global Climate in 2019, WMO-No. 1. ed. Chair, Publications Board, 7 bis, avenue de la Paix. P.O. Box 2300. CH-1211 Geneva 2, Switzerland.

Kljun, N., Calanca, P., Rotach, M.W., Schmid, H.P., 2004. A simple parameterisation for flux footprint predictions. Boundary-Layer Meteorol 112, 503–523. https://doi.org/10.1023/B:BOUN.0000030653.71031.96.

Knipper, K.R., Kustas, W.P., Anderson, M.C., Nieto, H., Alfieri, J.G., Prueger, J.H., Hain, C.R., Gao, F., McKee, L.G., Alsina, M.M., Sanchez, L., 2020. Using high-spatiotemporal thermal satellite ET retrievals to monitor water use over California vineyards of different climate, vine variety and trellis design. Agric. Water Manag. 241, 106361 https://doi.org/10.1016/j.agwat.2020.106361.

Kustas, W.P., Nieto, H., Morillas, L., Anderson, M.C., Alfieri, J.G., Hipps, L.E., Villagarcía, L., Domingo, F., Garcia, M., 2016. Revisiting the paper "Using radiometric surface temperature for surface energy flux estimation in Mediterranean drylands from a two-source perspective. Remote Sens. Environ. 184, 645–653. https://doi.org/10.1016/j.rse.2016.07.024.

Kustas, W.P., Norman, J.M., 2000. A two-source energy balance approach using directional radiometric temperature observations for sparse canopy covered surfaces. Agron. J. 92, 847–854.

Kustas, W.P., Norman, J.M., 1999. Evaluation of soil and vegetation heat flux predictions using a simple two-source model with radiometric temperatures for partial canopy cover. Agric. For. Meteorol. 94, 13–29. https://doi.org/10.1016/S0168-1923(99)00005-2.

Le Page, M., Toumi, J., Khabba, S., Hagolle, O., Tavernier, A., Kharrou, Hakim, M, Er-Raki, S, Huc, M, Kasbani, M, Moutamanni, El, A., Yousfi, M., Jarlan, L., 2014. A life-size and near real-time test of irrigation scheduling with a sentinel-2 like time series (SPOT4-Take5) in Morocco. Remote Sens. 6, 11182–11203. https://doi.org/10.3390/rs61111182.

Lionello, P., Scarascia, L., 2018. The relation between climate change in the Mediterranean region and global warming. Reg. Environ. Chang. 18, 1481–1493. https://doi.org/10.1007/s10113-018-1290-1.

Louis, J., Debaecker, V., Pflug, B., Main-Knorn, M., Bieniarz, J., Mueller-Wilm, U., Cadau, E., Gascon, F., 2016. Sentinel-2 SEN2COR: L2A Processor for Users. Eur. Sp. Agency, (Special Publ. ESA SP SP-740.

MAPA, 2019. Encuesta sobre Superficies y Rendimientos de Cultivos. Ministerio de Agricultura, Pesca y Alimentación, Gobierno de España.

Masson-Delmotte, V., Zhai, P., Pörtner, H.-O., Roberts, D., Skea, J., Shukla, P.R., Pirani, A., Moufouma-Okia, W., Péan, C., Pidcock, R., Connors, S., Matthews, J.B.R., Chen, Y., Zhou, X., Gomis, M.I., Lonnoy, E., Maycock, T., Tignor, M., Waterfield, T., 2018. IPCC, 2018: Global Warming of 1.5°C. An IPCC Special Report on the Impacts of Global Warming of 1.5°C above pre-industrial levels and related global greenhouse gas emission pathways, in the context of strengthening the global response to the threat of cli 1–630.

Mauder, M., Cuntz, M., Drüe, C., Graf, A., Rebmann, C., Schmid, H.P., Schmidt, M., Steinbrecher, R., 2013. A strategy for quality and uncertainty assessment of long-term eddy-covariance measurements. Agric. For. Meteorol. 169, 122–135. https://doi.org/10.1016/j.agrformet.2012.09.006.

Moderow, U., Aubinet, M., Feigenwinter, C., Kolle, O., Lindroth, A., Mölder, M., Bernhofer, C., 2009. Available energy and energy balance closure at four coniferous forest sites across. Europe. Theoretical and Applied Climatology 98 (3), 397–412. https://doi.org/10.1007/S00704-009-0175-0, 2009 98:3.

Mokhtari, A., Noory, H., Pourshakouri, F., Haghighatmehr, P., Afrasiabian, Y., Razavi, M., Fereydooni, F., Sadeghi Naeni, A., 2019. Calculating potential evapotranspiration and single crop coefficient based on energy balance equation using Landsat 8 and Sentinel-2. ISPRS J. Photogramm. Remote Sens. 154, 231–245. https://doi.org/10.1016/j.isprsjprs.2019.06.011.

Moncrieff, J., Clement, R., Finnigan, J., Meyers, T., 2004. Averaging, detrending, and filtering of eddy covariance time series. In: Lee, X., Massman, W., Law, B. (Eds.), Handbook of Micrometeorology. Atmospheric and Oceanographic Sciences Library. Kluwer Academic Publishers, Dordrecht, pp. 7–31. https://doi.org/10.1007/1-4020-2265-4_2. Vol 29.

Morcrette, J.J., Boucher, O., Jones, L., Salmond, D., Bechtold, P., Beljaars, A., Benedetti, A., Bonet, A., Kaiser, J.W., Razinger, M., Schulz, M., Serrar, S., Simmons, A.J., Sofiev, M., Suttie, M., Tompkins, A.M., Untch, A., 2009. Aerosol analysis and forecast in the European centre for medium-range weather forecasts integrated forecast system: forward modeling. J. Geophys. Res. Atmos. 114, 1–17. https://doi.org/10.1029/2008JD011235.

Norman, J.M., Anderson, M.C., Kustas, W.P., French, A.N., Mecikalski, J., Torn, R., Diak, G.R., Schmugge, T.J., Tanner, B.C.W., 2003. Remote sensing of surface energy fluxes at 10^{1} -m pixel resolutions. Water Resour. Res. 39, 1221. https://doi.org/10.1029/2002WR001775.

Norman, J.M., Kustas, W.P., Humes, K.S., 1995. Source approach for estimating soil and vegetation energy fluxes in observations of directional radiometric surface temperature. Agric. For. Meteorol. 77, 263–293. https://doi.org/10.1016/0168-1923(95)02265-Y.

Nyolei, D., Nsaali, M., Minaya, V., van Griensven, A., Mbilinyi, B., Diels, J., Hessels, T., Kahimba, F., 2019. High resolution mapping of agricultural water productivity using SEBAL in a cultivated African catchment. Tanzania. Phys. Chem. Earth 112, 36–49. https://doi.org/10.1016/j.pce.2019.03.009.

Olivera-Guerra, L., Mattar, C., Merlin, O., Durán-Alarcón, C., Santamaría-Artigas, A., Fuster, R., 2017. An operational method for the disaggregation of land surface temperature to estimate actual evapotranspiration in the arid region of Chile. ISPRS J. Photogramm. Remote Sens. 128, 170–181. https://doi.org/10.1016/j.isprsjprs.2017.03.014.

Ortega-Farías, S., Ortega-Salazar, S., Poblete, T., Kilic, A., Allen, R., Poblete-Echeverría, C., Ahumada-Orellana, L., Zuñiga, M., Sepúlveda, D., 2016. Estimation of energy balance components over a drip-irrigated olive orchard using thermal and multispectral cameras placed on a helicopter-based unmanned aerial vehicle (UAV). Remote Sens. 8, 1–18. https://doi.org/10.3390/rs8080638.

Overgaard, J., Rosbjerg, D., Butts, M.B., 2006. Land-surface modelling in hydrological perspective - a review. Biogeosciences 3, 229–241. https://doi.org/10.5194/bg-3-229-2006.

Paço, T.A., Pôças, I., Cunha, M., Silvestre, J.C., Santos, F.L., Paredes, P., Pereira, L.S., 2014. Evapotranspiration and crop coefficients for a super intensive olive orchard. An application of SIMDualKc and METRIC models using ground and satellite observations. J. Hydrol. 519, 2067–2080. https://doi.org/10.1016/j.jhydrol.2014.09.075.

Pakparvar, M., Cornelis, W., Pereira, L.S., Gabriels, D., Hosseinimarandi, H., Edraki, M., Kowsar, S.A., 2014. Remote sensing estimation of actual evapotranspiration and crop coefficients for a multiple land use arid landscape of southern Iran with limited available data. J. Hydroinformatics 16, 1441–1460. https://doi.org/10.2166/hydro.2014.140.

Parry, C.K., Nieto, H., Guillevic, P., Agam, N., Kustas, W.P., Alfieri, J., McKee, L., McElrone, A.J., 2019. An intercomparison of radiation partitioning models in vineyard canopies. Irrig. Sci. https://doi.org/10.1007/s00271-019-00621-x, 0, 0.

Pasqualotto, N., D'Urso, G., Bolognesi, S.F., Belfiore, O.R., Van Wittenberghe, S., Delegido, J., Pezzola, A., Winschel, C., Moreno, J., 2019. Retrieval of evapotranspiration from sentinel-2: Comparison of vegetation indices, semi-empirical models and SNAP biophysical processor approach. Agronomy 9. https://doi.org/10.3390/agronomy9100663.

Perez, R., Ineichen, P., Moore, K., Kmiecik, M., Chain, C., George, R., Vignola, F., 2002. A new operational model for satellite-derived irradiances: description and validation. Sol. Energy 73, 307–317. https://doi.org/10.1016/S0038-092X(02)00122-6.

Pôças, I., Paço, T.A., Cunha, M., Andrade, J.A., Silvestre, J., Sousa, A., Santos, F.L., Pereira, L.S., Allen, R.G., 2014. Satellite-based evapotranspiration of a super-intensive olive orchard: application of METRIC algorithms. Biosyst. Eng. 128, 69–81. https://doi.org/10.1016/j.biosystemseng.2014.06.019.

Priestley, C.H.B., Taylor, R.J., 1972. On the assessment of surface heat flux and evaporation using large-scale parameters. Mon. Weather Rev. 100, 81–92. https://doi.org/10.1175/1520-0493(1972)100<0081:OTAOSH>2.3.CO;2.

Reichstein, M., Falge, E., Baldocchi, D., Papale, D., Aubinet, M., Berbigier, P., Bernhofer, C., Buchmann, N., Gilmanov, T., Granier, A., Grunwald, T., Havrankova, K., Ilvesniemi, H., Janous, D., Knohl, A., Laurila, T., Lohila, A., Loustau, D., Matteucci, G., Meyers, T., Miglietta, F., Ourcival, J.-M., Pumpanen, J., Rambal, S., Rotenberg, E., Sanz, M., Tenhunen, J., Seufert, G., Vaccari, F., Vesala, T., Yakir, D., Valentini, R., 2005. On the separation of net ecosystem exchange into assimilation and ecosystem respiration: review and improved algorithm. Glob. Chang. Biol. 11, 1424–1439. https://doi.org/10.1111/j.1365-2486.2005.001002.x.

Santanello, J.A., Friedl, M.A., 2003. Diurnal Covariation in Soil Heat Flux and Net Radiation. J. Appl. Meteorol. 42, 851–862. https://doi.org/10.1175/1520-0450(2003)042<0851:DCISHF>2.0.CO;2.

Schmid, H.P., 2002. Footprint modeling for vegetation atmosphere exchange studies: A review and perspective. Agric. For. Meteorol. 113, 159–183. https://doi.org/10.1016/S0168-1923(02)00107-7.

Shukla, P.R., Skea, J., Buendia, E.C., Masson-Delmotte, V., Pörtner, H.-O., Roberts, D.C., Zhai, P., Slade, R., Connors, S., Diemen, R.van, Ferrat, M., Haughey, E., Luz, S., Neogi, S., Pathak, M., Petzold, J., Pereira, J.P., Vyas, P., Huntley, E., Kissick, K., M, J. M., 2019. Climate Change and Land: an IPCC special report on climate change, desertification, land degradation, sustainable land management, food security, and greenhouse gas fluxes in terrestrial ecosystems.

Shuttleworth, W.J., Wallace, J.S., 1985. Evaporation from sparse crops-an energy combination theory. Q. J. R. Meteorol. Soc. 111, 839–855. https://doi.org/10.1002/qj.49711146910.

UNDRR, 2019. Global Assessment Report on Disaster Risk Reduction. Geneva, Switzerland.

UNESCO, UN-Water, 2020. 2020. United Nations World Water Development Report 2020. Paris.

Vickers, D., Mahrt, L., 1997. Quality control and flux sampling problems for tower and aircraft data. J. Atmos. Ocean. Technol. 14, 512–526. https://doi.org/10.1175/1520-0426(1997)014<0512:QCAFSP>2.0.CO;2.

Weiss, M., Baret, F., 2016. Sentinel2 ToolBox Level2 Products: LAI, FAPAR, FCOVER Version 1.1.

Zhan, W., Chen, Y., Zhou, J., Wang, J., Liu, W., Voogt, J., Zhu, X., Quan, J., Li, J., 2013. Disaggregation of remotely sensed land surface temperature: literature survey, taxonomy, issues, and caveats. Remote Sens. Environ. https://doi.org/10.1016/j.rse.2012.12.014.